ARTICLES
https://doi.org/10.1038/s41566-021-00882-z

nature photonics

Check for updates

Magnetic-free silicon nitride integrated optical isolator

Hao Tian[1,3], Junqiu Liu[2,3], Anat Siddharth[2], Rui Ning Wang[2], Terence Blésin[2], Jijun He[2], Tobias J. Kippenberg[2]✉ and Sunil A. Bhave[1]✉

Integrated photonics enables signal synthesis, modulation and conversion using photonic integrated circuits (PICs). Many materials have been developed, among which silicon nitride (Si_3N_4) has emerged as a leading platform particularly for nonlinear photonics. Low-loss Si_3N_4 PICs have been widely used for frequency comb generation, narrow-linewidth lasers, microwave photonics and photonic computing networks. Yet, among all demonstrated functionalities for Si_3N_4 integrated photonics, optical non-reciprocal devices such as isolators and circulators have not been achieved. Conventionally, they are realized based on the Faraday effect of magneto-optic materials under an external magnetic field; however, it has been challenging to integrate magneto-optic materials that are not compatible with complementary metal–oxide–semiconductors and that require bulky external magnet. Here we demonstrate a magnetic-free optical isolator based on aluminium nitride (AlN) piezoelectric modulators monolithically integrated on low-loss Si_3N_4 PICs. The transmission reciprocity is broken by spatio-temporal modulation of a Si_3N_4 microring resonator with three AlN bulk acoustic wave resonators that are driven with a rotational phase. This design creates an effective rotating acoustic wave that allows indirect interband transition in only one direction among a pair of strongly coupled optical modes. A maximum of 10 dB isolation is achieved under 300 mW total radiofrequency power applied to three actuators, with minimum insertion loss of 0.1 dB. An isolation bandwidth of 700 MHz is obtained, determined by the optical resonance linewidth. The isolation remains constant over nearly 30 dB dynamic range of optical input power, showing excellent optical linearity. Our integrated, linear, magnetic-free, electrically driven optical isolator could be a key building block for integrated lasers and optical interfaces for superconducting circuits.

Integrated photonics has enabled chip-scale optical systems with compact sizes, portable weight and low power consumption, which have been translated from table-top research set-ups to commercial products. With the advancement of nanofabrication technology, there have been major achievements in integrated semiconductor lasers[1,2] and modulators[3–8], as well as ultralow-loss PICs[9–13]. Importantly, the nonlinearities of ultralow-loss PICs have been explored and harnessed[14,15], giving rise to nonlinear photonics such as optical frequency comb generation[16]. Formed in Kerr-nonlinear optical microresonators, dissipative Kerr soliton (DKS) microcombs[15,16] constitute miniaturized, coherent, broadband optical frequency combs with repetition rates in the millimetre-wave to microwave domain and are amenable to heterogeneous integration with III–V/Si lasers[2]. Major progress has been made in the past decade in developing various platforms, including Si_3N_4 (refs. [11–13]), $LiNbO_3$ (refs. [17,18]), AlN (refs. [19,20]) and AlGaAs (refs. [10,21]). Among the materials developed thus far for integrated nonlinear photonics, Si_3N_4 has become the leading platform due to its exceptionally low loss (down to 1 dB m^{-1}), high Kerr nonlinearity, absence of two-photon absorption and high power handling capability. Indeed, most of the system-level demonstrations of DKS microcombs have been based on Si_3N_4. Meanwhile, high-Q Si_3N_4 microresonators have also been used recently to create ultralow-noise semiconductor lasers[2,22] whose performance is on par with advanced fibre lasers.

Despite such advances in Si_3N_4 integrated photonics, non-reciprocal devices, such as isolators and circulators that are widely used in optical communications and data centres for signal routing, multiplexing, and protecting lasers from reflections, have not been improved via these developments. Conventionally, optical non-reciprocity is realized in magneto-optic materials[23] where the Faraday effect induces non-reciprocal polarization rotation under external magnetic field. However, magneto-optic materials are not complementary metal–oxide–semiconductor (CMOS) compatible, posing challenges to integrate using standard CMOS techniques developed for silicon photonics. Besides, the magneto-optic effect is weak from the near-infrared to visible wavelength range, therefore requiring a strong external magnetic field applied at microscopic scale. Nevertheless, successful integration of cerium-substituted yttrium iron garnet (Ce:YIG) on PICs (for example, on silicon[24,25] or Si_3N_4 (ref. [26])) has been demonstrated via wafer bonding or deposition, though these efforts suffer from substantial optical losses and external magnet. Moreover, the requirement of large magnetic field bias makes it incompatible with superconducting qubits where optical isolation is needed for blocking reflected noises in optical interfaces for quantum interconnects[27].

To overcome these bottlenecks, magnetic-free schemes have been demonstrated to break Lorentz reciprocity and time-reversal symmetry, through synthetic magnetic field[28–31], optical nonlinearities[32–38], optomechanically induced transparency[39–42] and stimulated Brillouin scattering[43–47]; however, challenges remain in all of these approaches. For example, optomechanically induced non-reciprocity requires air-cladded, isolated microtoroids or microspheres that are difficult to integrate with PICs. Furthermore, the isolation bandwidth is primarily limited by the mechanical resonance linewidth, which is typically within the kilohertz to megahertz range. Separating the signal from the control pump laser using common multiplexing schemes is a formidable challenge, as they are spaced by the mechanical resonance that is typically below hundred

[1]OxideMEMS Lab, Purdue University, West Lafayette, IN, USA. [2]Institute of Physics, Swiss Federal Institute of Technology Lausanne (EPFL), Lausanne, Switzerland. [3]These authors contributed equally to the work. Hao Tian and Junqiu Liu. ✉e-mail: tobias.kippenberg@epfl.ch; bhave@purdue.edu

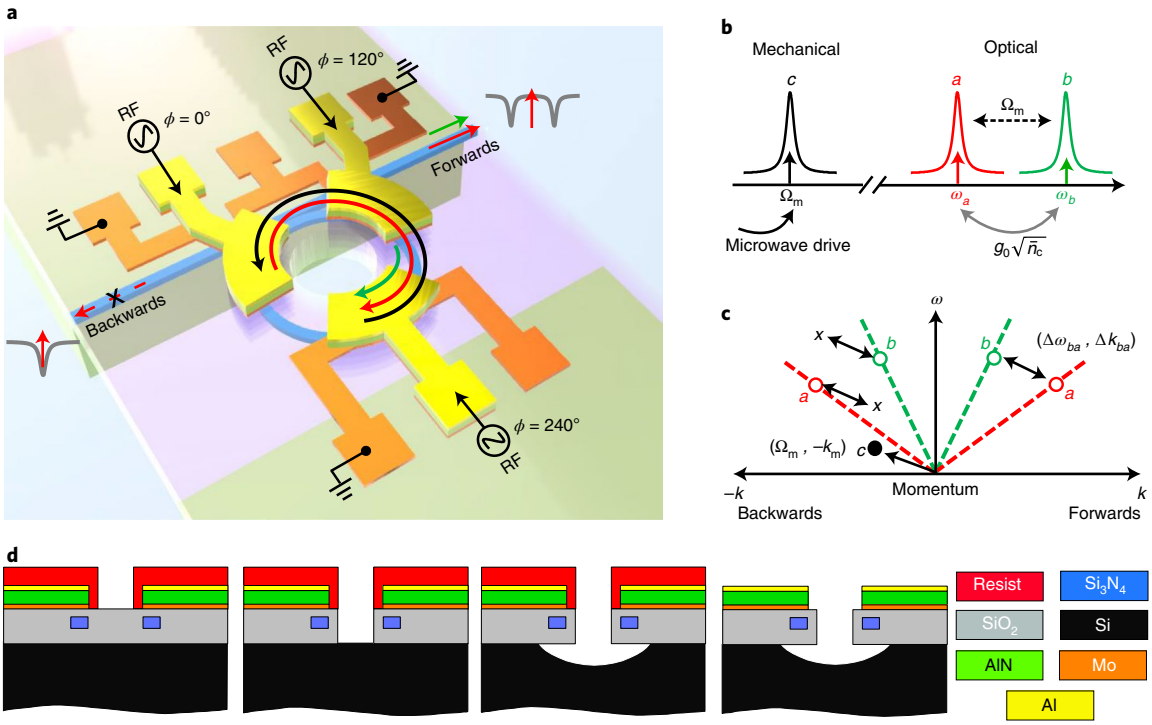

Fig. 1 | Principle of the nitride optical isolator. a, A schematic and device rendering. Three discrete AlN piezoelectric actuators are equidistantly integrated on top of a Si_3N_4 microring resonator (blue). When coherently driving these actuators with fixed relative phases $(\phi_1, \phi_2, \phi_3) = (0°, 120°, 240°)$, a rotating acoustic wave (black arrow) is generated that spatio-temporally modulates the two co-propagating optical modes (red and green arrows), leading to indirect interband transition in only one direction where the phase matching condition is fulfilled. **b**, A frequency-domain representation illustrating the indirect interband transition. When the two optical modes (*a* and *b*) are spaced by the resonant frequency Ω_m of the mechanical mode *c* (that is, $\Delta\omega_{ba} = \omega_b - \omega_a = \Omega_m$), scattering among modes *a* and *b* happens with a scattering rate of $g = g_0\sqrt{\bar{n}_c}$ under a microwave drive at Ω_m. **c**, A schematic of $\omega - k$ space showing the phase matching condition, that is, the energy ($\Delta\omega_{ba} = \Omega_m$) and momentum ($\Delta k_{ba} = -k_m$) conservations. Interband transition that couples the two optical modes with the acoustic wave is only allowed in the direction where phase matching condition is fulfilled, giving rise to transparency on resonance in this direction (forward, as shown in **a**) and extinction in the other direction (backward). **d**, Fabrication process flow to suspend the SiO_2 membrane where the Si_3N_4 microring resonator is embedded, to enhance the optomechanical coupling. The key technique used here is a silicon isotropic dry etching using SF_6 Bosch process.

megahertz. Although nonlinear optics can work passively without active modulation, the main concern is the dynamic reciprocity that forbids light propagation in both directions with limited dynamic range of input optical power[48].

Spatio-temporal modulation[49–55], which breaks reciprocity by coupling two optical modes and prescribing phase matching condition by active modulation, stands out in terms of integration and applicability on nearly all optical materials. Schemes based on acousto-optic modulation (AOM) have recently been extensively developed due to their compatibility with low-loss PICs (for example, AlN[54] and silicon[55]). Thus far, only non-reciprocal sideband modulation is achieved, limited by the modulation efficiency and power handling capability of the interdigital transducers for generating surface acoustic waves. Here we demonstrate the first AOM-based optical isolator for Si_3N_4 integrated photonics. Three AlN piezoelectric actuators are equidistantly placed along a Si_3N_4 microring resonator, and generate high-overtone bulk acoustic resonances (HBAR)[5] to create an effective rotating acoustic wave that couples two optical modes only in the momentum-biased direction.

Results

Device principle and design. Our integrated optical isolator consists of three AlN piezoelectric actuators on top of a Si_3N_4 microring resonator, as shown in Fig. 1a. The Si_3N_4 PIC (blue) fully cladded with SiO_2 was fabricated using the photonic Damascene process[13], followed by monolithic integration of AlN actuators[5,6]. Figure 1d shows the fabrication process flow, and more details are found in Methods. The AlN thin film (green) with a piezoelectric coefficient of $d_{33} = 3.9\,\mathrm{pm\,V^{-1}}$ is sandwiched between the aluminium (top, yellow) and molybdenum (bottom, orange) electrodes. When the electrodes are microwave-driven, bulk acoustic waves are formed vertically in the substrate (that is, the HBAR mode) beneath the actuators. By contrast to previous work[5], here we apply a silicon release process to create a suspended SiO_2 membrane in which Si_3N_4 microresonator is embedded. This release process enables tight confinement of HBAR modes inside the Fabry–Pérot acoustic cavity formed by the top and bottom SiO_2–air surfaces, and thus enhances the acousto-optic coupling through stress-optic effect[5].

The Si_3N_4 microresonator is designed to support two optical eigenmodes (*a* and *b*) at a frequency difference that matches a mechanical/acoustic resonant frequency, as shown in Fig. 1b. The microwave drives applied on the three AlN actuators create acoustic waves inside the mechanical cavity, which scatter light between modes *a* and *b* (that is, indirect interband transition). Figure 1c illustrates the $\omega - k$ space, where $k = 2\pi/\lambda$ is wavenumber (the photon/phonon momentum is $\hbar k$, with the sign denoting the rotating direction along the microring, clockwise or counter-clockwise), and ω is the angular frequency. To induce interband transition, energy and momentum conservations must be satisfied, known as the phase matching condition. With a non-zero phonon momentum k_m, phase matching requires $\Delta\omega_{ba} = \omega_b - \omega_a = \Omega_m$ and $\Delta k_{ba} = k_b - k_a = -k_m$, where $\Delta\omega_{ba}$ is the optical frequency spacing, and the minus sign of

k_m indicates that the acoustic wave counter-propagates with the two co-propagating optical modes, as illustrated in Fig. 1a. We denote this direction of light transmission—where phase matching condition is fulfilled—as the forward direction in the following discussion.

While a single vertical HBAR mode from one AlN actuator carries zero in-plane momentum, an effective acoustic wave rotating along the microring is generated by driving three actuators coherently with phases of (0°, 120°, 240°), that is, a 120° phase difference between the two adjacent actuators, as illustrated in Fig. 1a. In the forward direction, the two optical modes are coupled via the rotating acoustic wave, which can be described by simplified coupled-mode theory (CMT) equations[56]:

$$\frac{d}{dt}\hat{a} = -(i\Delta_a + \frac{\kappa_a}{2})\hat{a} - ig\hat{b}e^{i\Omega_d t} + \sqrt{\kappa_{a,ex}}\hat{a}_{in} \quad (1)$$

$$\frac{d}{dt}\hat{b} = -(i\Delta_b + \frac{\kappa_b}{2})\hat{b} - ig\hat{a}e^{-i\Omega_d t} \quad (2)$$

where $\hat{a}(\hat{b})$ is the intracavity amplitude, κ_a (κ_b) is the total loss rate of mode a (b), $\kappa_{a,ex}$ is the external coupling rate of mode a. These equations of motion are transformed under the rotating-wave approximation referenced to the input laser frequency $\omega_L/2\pi$, thus $\Delta_a = \omega_a - \omega_L$ ($\Delta_b = \omega_b - \omega_L$) is the relative detuning between the laser frequency and the optical resonant frequency of a (b); $\Omega_d/2\pi$ is the microwave drive frequency, which can be slightly detuned from the mechanical resonant frequency $\Omega_m/2\pi$. Mode a is probed by the input light with amplitude $\hat{a}_{in}$, and its optical transmission/isolation is studied in the following analysis.

In the forward direction, the two optical modes undergo interband transition with a scattering rate $g = g_0\sqrt{\bar{n}_c}$, where g_0 is the single photon-phonon coupling rate describing the optomechanical interaction strength, and $\bar{n}_c$ is the steady-state intracavity phonon number; $C = 4g^2/\kappa_a\kappa_b$ is the photon–photon cooperativity, which measures the ratio of scattering rate to optical losses. Strong coupling requires $C \gg 1$, which can induce Rabi oscillation and mode splitting. The latter results in a transparency window on the resonance in the light transmission, which can be calculated from equations (1) and (2) as:

$$T|_{\Delta_a = 0} = \left|\frac{\hat{a}_{out}}{\hat{a}_{in}}\right|^2_{\Delta_a = 0} = \left[1 - \frac{2\kappa_{a,ex}}{\kappa_a(1+C)}\right]^2 \quad (3)$$

In the forward direction, $C \gg 1$ and $T|_{\Delta_a = 0} = 1$. This transparency can be understood intuitively as the impedance mismatch between the bus waveguide and the microresonator which results from the increasing effective intrinsic loss due to the scattering to the other optical mode b. In the backward direction where the three-wave phase matching is not fulfilled, interband transition is prohibited, leading to $C \approx 0$ and $T|_{\Delta_a = 0} = 0$ in the critical coupling regime ($\kappa_a = 2\kappa_{a,ex}$). Consequently, the microresonator remains critically coupled and its light transmission is not affected by the presence of the acoustic wave. This non-reciprocal transmission between the forward ($T = 1$) and backward ($T = 0$) directions is the basic of our optical isolator.

Meanwhile, in the forward direction, a single modulation sideband is generated in mode b, which is frequency-shifted by $\Omega_d/2\pi$ relative to $\omega_L/2\pi$. The mode conversion efficiency η is:

$$\eta|_{\Delta_a = 0} = \left|\frac{\hat{b}_{out}}{\hat{a}_{in}}\right|^2_{\Delta_a = 0} = \frac{\kappa_{a,ex}}{\kappa_a}\frac{\kappa_{b,ex}}{\kappa_b}\frac{4C}{(1+C)^2} \quad (4)$$

Equations (3) and (4) are derived assuming that the microwave drive Ω_d matches $\Delta\omega_{ba}$, that is $\Omega_d = \Delta\omega_{ba}$. A detailed derivation of these equations and general cases with a frequency mismatch—which were used for subsequent fitting with experiments—are provided in Methods. This non-reciprocal sideband generation has been demonstrated in previous studies in the $C < 1$ regime[53–55].

Device characterization. Figure 2a shows a false-coloured, top-view, scanning electron microscope (SEM) image of the fabricated device with three AlN actuators integrated onto a released Si_3N_4 microring resonator. The thickness of Al/AlN/Mo is 100/1,000/100 nm, respectively. The sulfur hexafluoride (SF_6) Bosch process was used to isotropic dry etch the silicon after opening the centre hole by oxide etching, allowing partial removal of the silicon substrate and the suspension of 5.4-μm-thick SiO_2 cladding. Figure 2b shows the optical microscope image highlighting the bus waveguide coupling region, the Si_3N_4 microring with a 118-μm-radius buried in the suspended SiO_2 membrane, and two AlN actuators. Figure 2c shows the simulated stress distribution of one HBAR mode within the SiO_2 membrane using finite element method. It can be seen that the HBAR mode is uniformly distributed under the AlN actuator and tightly confined in the SiO_2 membrane, allowing direct modulation of the optical mode propagating along the waveguide through photoelastic and moving boundary effects[57,58].

We use the fundamental transverse electric (TE_{00}, that is, mode a) and magnetic modes (TM_{00}, that is, mode b) to realize interband transition assisted with the rotating acoustic wave. A quasi-square waveguide cross-section ($810 \times 820\,nm^2$) is used, as shown in the inset of Fig. 2b. Figure 2c shows the simulated TE_{00} and TM_{00} mode profiles, which also include the slanted waveguide sidewalls. The transmission of polarization-tilted light through the optical microresonator, including a pair of TE_{00} and TM_{00} resonances, is shown in Fig. 2d. The TM_{00} mode frequency is 3 GHz higher than that of the TE_{00} mode at around 1,546 nm wavelength. The resonance linewidth (total loss, $\kappa_{a,b}/2\pi$) is 0.68 and 1.16 GHz for the TE_{00} and TM_{00} modes, respectively.

Figure 2e shows the microwave reflection S_{11}, where mechanical resonances are revealed. Only one actuator's S_{11} is shown as the others are similar. Three strong resonances are found at around 3.0, 3.4 and 3.8 GHz, which are due to the SiO_2 mechanical cavity with ~470 MHz free spectral range (FSR, determined by the SiO_2 cladding thickness). Besides, weak resonances with an FSR of ~19 MHz are observed, due to the HBARs in the thick silicon substrate formed under square signal probe pads which were not undercut[5]. However, only the HBARs confined in SiO_2 can efficiently modulate the optical mode because the HBARs in the silicon substrate have negligible overlap with the Si_3N_4 waveguide, which can be verified from the optomechanical S_{21} response shown in Fig. 2e. S_{21} measures the ratio between the output light intensity modulation and the microwave drive power. Three actuators are measured individually. As the HBARs are mainly determined by the thickness of each layer that is highly uniform over the device scale, the HBAR frequencies of the three actuators show only sub-megahertz misalignment. A maximum of −45 dB S_{21} is achieved, providing 20 dB improvement over a previously reported unreleased silicon HBAR AOM[5]. This is due to the considerably reduced mechanical mode volume and tighter HBAR confinement in the released SiO_2 membrane. The SiO_2 HBAR at 2.958 GHz is used in the following experiments to match the optical mode spacing. Furthermore, the signal cross-talk between the actuators is maintained below −60 dB (see Supplementary Note 6), as the HBARs are tightly confined vertically beneath the actuator, and the centre etched hole prevents the transmission of any lateral mechanical modes.

Optical isolation demonstration. The experimental set-up is shown in Fig. 3a. Three radiofrequency (RF) signals are amplified and applied to each actuator, and the amplitudes and phases of each channel are controlled individually by each signal generator.

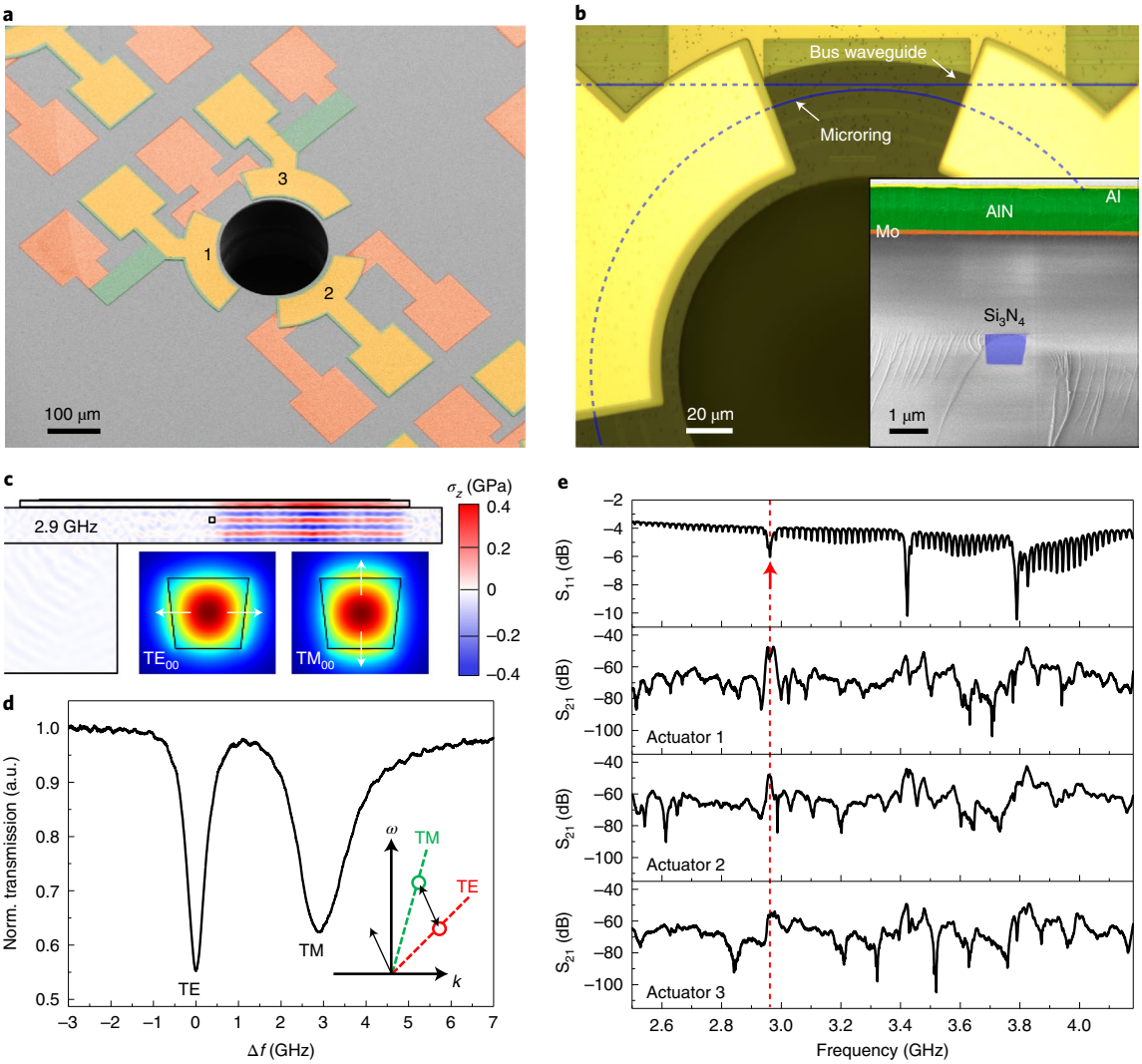

Fig. 2 | Characterization of optical and mechanical properties of the isolator device. a, A false-coloured top-view SEM image of the fabricated device. **b**, An optical microscope image highlighting the bus–microring coupling section, the released SiO_2 area, and the relative positions of Si_3N_4 waveguides (blue lines) and two AlN actuators. The inset is a false-coloured SEM image of the sample cross-section, showing the vertical structure of the piezoelectric actuator and quasi-square Si_3N_4 photonic waveguide. **c**, Finite element method numerical simulations of the vertical stress σ_z distribution of a typical HBAR mode at 2.9 GHz, and the optical profiles of the TE_{00} and TM_{00} modes of the quasi-square Si_3N_4 waveguide. White arrows mark the optical polarization directions. **d**, An optical transmission spectrum showing a pair of TE_{00} and TM_{00} modes with around 3 GHz frequency spacing. The *x*-axis is frequency-calibrated relative to the centre frequency of the TE_{00} mode around 1,546 nm. Inset shows the relative position of the two modes in the $\omega - k$ space. **e**, The top subpanel shows the microwave reflection S_{11}, whereas the next three show the optomechanical response S_{21} of actuators 1–3 (labelled in **a**), respectively. Red arrow marks the mechanical mode at 2.958 GHz that is used in the experiment.

The TE_{00} mode is excited by aligning the input light polarization using fibre polarization controllers (FPCs 1 and 2). The light propagation direction—forward or backward—is controlled by a 2×2 optical switch. The transmitted TE light and generated TM sideband are separated by a polarization beam splitter (PBS), which is a key reason why we use two modes of different polarizations. The laser wavelength is continuously scanned to probe the spectral response around the TE_{00} resonance.

The RF phases are critical for phase matching. Figure 3b shows the transmission spectrum of TE light by sweeping the RF phases of signals 2 and 3 relative to signal 1 (ϕ_{21} and ϕ_{31}), whereas the output RF power (20 dBm for each actuator) and light input direction are fixed. Note that reversing the sign of the RF phases changes the rotation direction of the acoustic wave. Non-reciprocity is seen from the disparate transmission by reversing the RF phases with respect to the origin (0°, 0°). Strong mode splitting is induced under ideal phase setting $(\phi_{21}, \phi_{31}) = (120°, -120°)$, while the original single resonance is maintained at $(\phi_{21}, \phi_{31}) = (-120°, 120°)$, as shown in Fig. 3d. When the RF phases deviate from the ideal values within ±30°, non-reciprocity only slightly degrades, which allows large tolerance of phase fluctuations in practical applications. This behaviour and RF phase dependency are also revealed by finite-difference frequency-domain (FDFD) simulations[52], showing qualitative agreement with experimental data (see Supplementary Note 4).

Light transmission of the generated anti-Stokes TM sideband is simultaneously measured as shown in Fig. 3c. It is normalized to the TE's input power, thus can be interpreted as conversion efficiency η. Figure 3b and 3c show similar patterns but with reversed colour rendering. Prominent splitting and TE–TM conversion are found at (120°, −120°), whereas TE–TM conversion is negligible at (−120°, 120°). As the measured TM sideband results from mode coupling

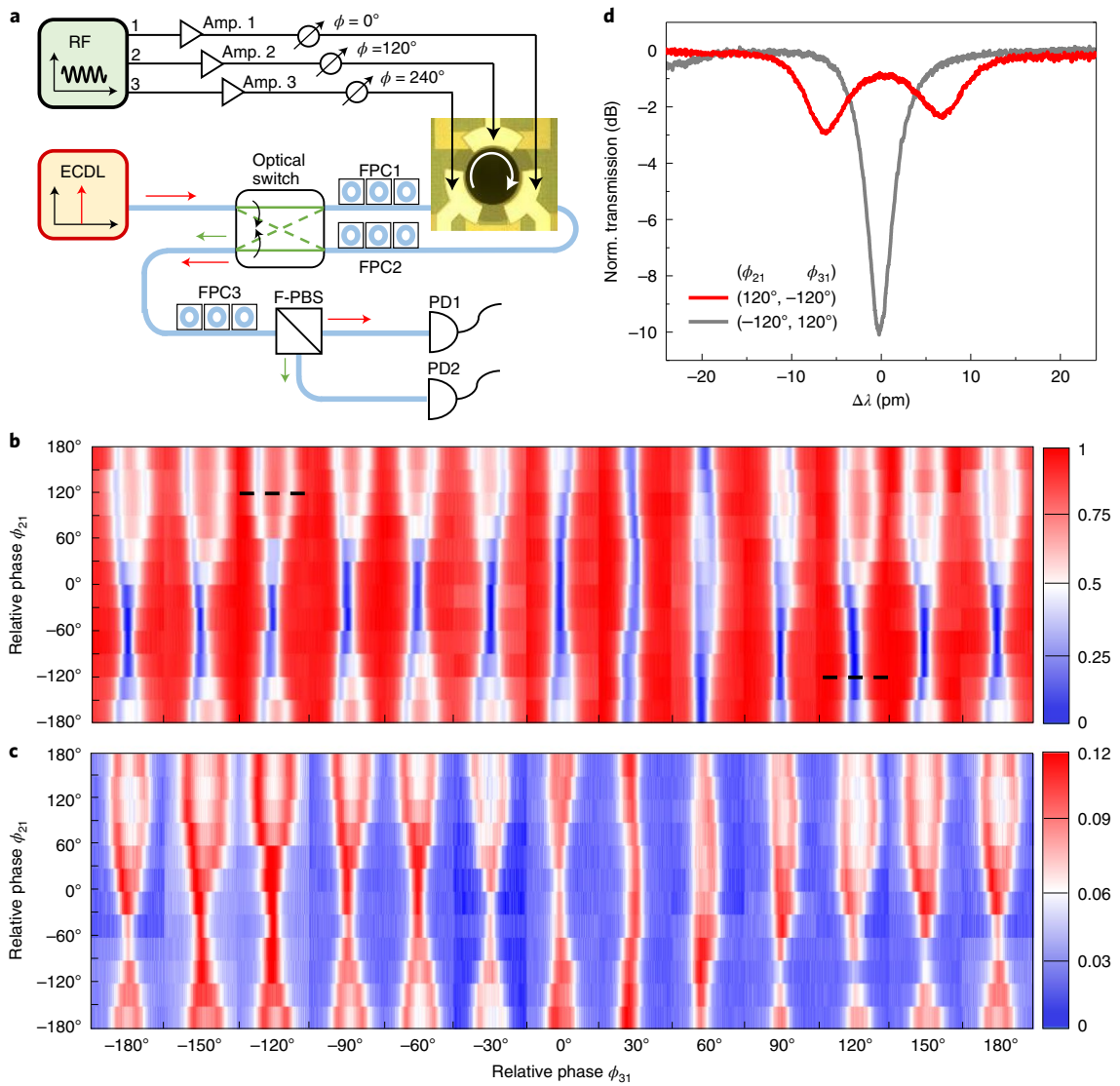

Fig. 3 | Optical isolation and radiofrequency phases dependency. a, Experimental set-up. Three RF signals are amplified and applied to the AlN actuators with phases controlled individually. An optical switch is used to control the direction of input TE light (red arrows). The output TE light (red arrows) and the generated TM sideband (green arrows) are spatially separated and detected. The white arrow on the device denotes the clockwise rotation of the RF drive in the forwards direction. Amp, RF amplifier; ECDL, external-cavity diode laser; FPC, fibre polarization controller; F-PBS, fibre polarization beam splitter; PD, photodetector. **b**,**c**, Optical transmission (**b**) and converted sideband (**c**) under phase sweep of signals 2 and 3 relative to signal 1, that is, ϕ_{21} and ϕ_{31}. Each column is an experimentally measured spectrum under the same ϕ_{31} with a spectral span of ±16 pm relative to the centre wavelength λ_0 (1,542.6 nm) of the TE_{00} mode. Both **b** and **c** are normalized to the input TE light power on chip. **d**, Optical transmission spectra with $(\phi_{21}, \phi_{31}) = (120°, -120°)$ (perfect phase matching, red) and $(\phi_{21}, \phi_{31}) = (-120°, 120°)$ (largest phase mismatch, grey). These two phase combinations are marked as black dashed lines in **b**.

and phase matching, it can be used as feedback signal for tuning and stabilizing the RF phases. From Fig. 3d, the optical isolation ratio between the clockwise (forward) and counter-clockwise (backward) directions is calculated as 9.3 dB, which is mainly limited by the level of critical coupling (−10.1 dB) of the optical microring (the current device is slightly undercoupled with 850 nm bus–microring gap). The isolation ratio can be improved in the future by fine tuning the bus–microring gap in the design and fabrication. We achieve 83% transmission on resonance corresponding to 0.8 dB insertion loss in the forward direction. We further note another device with 0.1 dB insertion loss (98% transmission), which shows higher modulation efficiency but less backward extinction due to the fact that the microring is more undercoupled with a wider gap (950 nm, see Supplementary Note 5).

Radiofrequency power dependency. The evolution of optical isolation with varying applied RF power is studied in Fig. 4 with fixed RF phases of $(\phi_{21}, \phi_{31}) = (120°, -120°)$ and a drive frequency of 2.968 GHz. Figure 4a shows the measured forward and backward transmissions of the TE_{00} mode, with the RF power (applied to each actuator) increased from 15 to 20 dBm. In the forward direction, initially the resonance depth decreases and the linewidth broadens with increasing RF power up to 16 dBm, resulted from the increasing intrinsic loss caused by the scattering to the TM_{00} mode. Above 17 dBm, mode splitting appears, creating a transparency window at the original resonance frequency. In the backward direction, single-resonance profile remains, however, with slightly increasing linewidth due to the weak mode coupling as predicted and described by the Floquet theorem[52]. Figure 4c shows the isolation

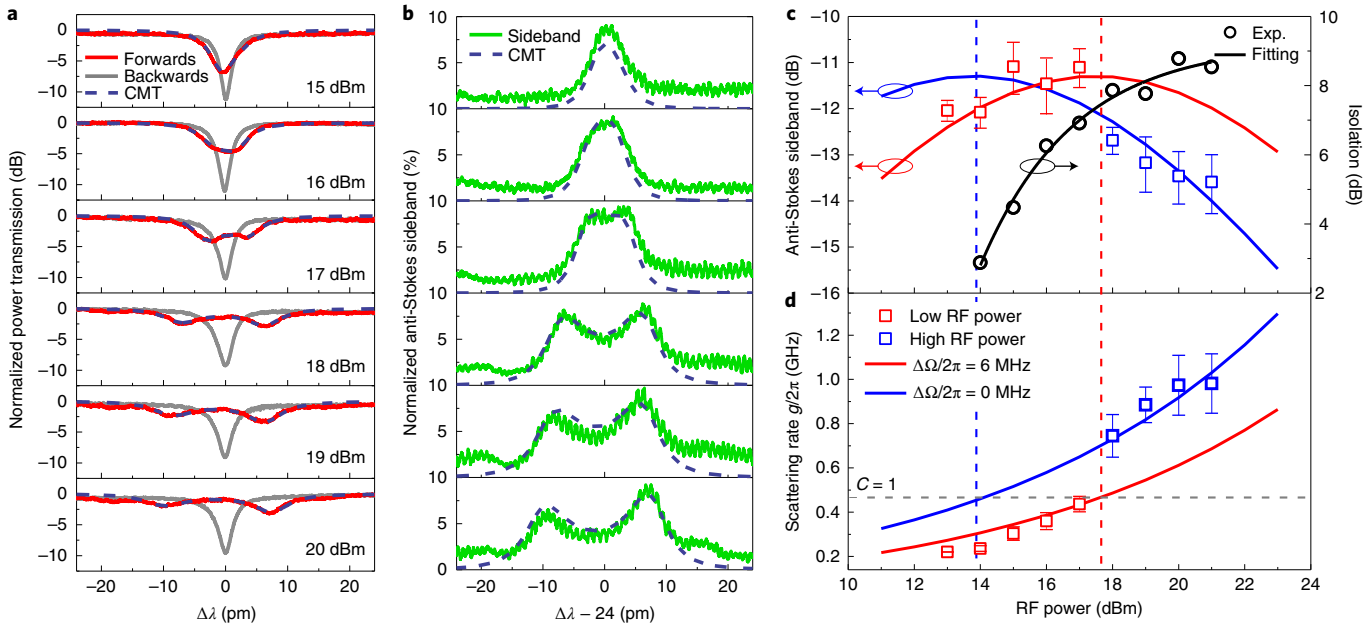

Fig. 4 | RF power dependency and anti-Stokes TM sideband generation. a, Optical transmission spectra of the TE light in the forward and backward directions, with increasing RF power from 15 to 20 dBm; $\Delta\lambda$ is the wavelength detuning of the input laser relative to the TE_{00} mode $\Delta\lambda = \lambda_L - \lambda_{TE,0}$, with $\lambda_{TE,0} = 1{,}544.1$ nm. **b**, Generated light of the anti-Stokes TM sideband in the forward direction, normalized by the input TE light power. The RF power increase is the same as **a**. The anti-Stokes sideband is blue-shifted relative to the input laser by the modulation frequency 2.968 GHz (~24 pm, $\lambda_{TM} - \lambda_{TE,0} = \Delta\lambda - 24$). The fitted transmission using CMT is also shown in **a** and **b**. **c**,**d**, The conversion efficiency of the TM sideband at $\Delta\lambda = 0$ and the scattering rate g as a function of RF power. Experimental data are grouped as low and high RF powers, fitted individually with CMT (solid lines) with different microwave drive to mechanical resonance detuning $\Delta\Omega = \Omega_d - \Omega_m$. The horizontal grey dashed line in **d** marks the value of $g/2\pi \approx 460$ MHz when cooperativity $C = 1$. The vertical red and blue dashed lines in **c** and **d** mark the maximum conversion at each detuning. The error bars of each data point represent the standard deviation (s.d.) from five individual measurements. The dependence of isolation on RF power is shown in **c** with experimental data and exponential fitting. Note that the RF power in all of the panels is the power applied to each individual actuator, thus the total RF power consumption is three times (4.8 dB) higher.

ratio (black circles) at zero laser detuning relative to the TE_{00} mode ($\Delta\lambda = 0$), which increases exponentially with the applied RF power and is finally limited by the backward extinction.

The mode splitting rate, which is two times of the interband scattering rate g, is extracted by fitting the resonance profile using the generalized equation (3) from CMT, with g and $\Delta\omega_{ba}$ as fitting parameters. Figure 4d shows that g gradually increases with increasing RF power and sharply increases to a higher value at 18 dBm, above which g continuously increases and finally saturates at 20 dBm. This behaviour is caused by the blue shift of the SiO_2 HBARs due to RF heating, as SiO_2 has a large positive temperature coefficient of elasticity of 188 ppm K^{-1}. The RF drive frequency Ω_d is initially blue-detuned from the HBAR frequency Ω_m at room temperature, that is, $\Omega_d - \Omega_m > 0$. As the RF power increases and the acoustic velocity in SiO_2 increases, Ω_m approaches Ω_d (that is, $\Omega_d - \Omega_m \to 0$) and more phonons are pumped into the mechanical cavity. This in turn increases the temperature, which further blue-shifts the HBAR. The thermal nonlinearity thus leads to an increase in g at approximately 18 dBm. This transition is studied in Supplementary Note 7 with a fine sweep of RF power in 0.1 dBm steps.

With RF power above 20 dBm, the interband scattering rate g saturates, indicating that the efficiency of pumping phonons into the cavity starts dropping. This is probably because Ω_d becomes red-detuned to Ω_m, that is, $\Omega_d - \Omega_m < 0$; thus, nearly zero detuning can be derived for RF powers between 18 and 20 dBm. In this regime, the single-phonon optomechanical coupling strength $g_0/2\pi$ is estimated as 208 Hz, by fitting high RF power data (blue line) with $g = g_0\sqrt{\bar{n}_c}$, where $\bar{n}_c$ is calculated by extracting the electromechanical coupling efficiency $k^2_{t,eff} = 0.2\%$ from S_{11} (see Supplementary Note 3). The low RF power region is fitted with $(\Omega_d - \Omega_m)/2\pi \approx 6$ MHz blue-detuning (red line). Another consequence of the RF heating effect is the drift of $\Delta\omega_{ba}$. Figure 4a shows that the mode splitting evolves from symmetric (18 dBm) to asymmetric (20 dBm) with increasing RF power, and $\Delta\omega_{ba}/2\pi$ is increased from 3 GHz to 3.3 GHz.

The spectrum of the anti-Stokes TM sideband is shown in Fig. 4b. The conversion efficiency η at zero laser detuning to the TE_{00} mode ($\Delta\lambda = 0$) is plotted in Fig. 4c. Similarly, each dataset with low and high RF power is fitted individually using equation (4) with the same RF driving detuning as used in Fig. 4d. It can be derived from equation (4) that the maximum value of η is reached at $C = 1$. This can also be seen from Fig. 4b where the conversion starts to drop at centre due to the mode splitting when $C > 1$. A maximum of 8% (−11 dB) of the TE_{00} mode power is converted into the TM_{00} sideband, which is mainly limited by the external coupling efficiency of the TE_{00} mode ($\kappa_{a,ex}/\kappa_a = 0.34$) and TM_{00} mode ($\kappa_{b,ex}/\kappa_b = 0.24$), see equation (4). At zero RF drive detuning (blue line), $C = 1$ is achieved with 14 dBm RF power applied on each actuator (18.8 dBm in total), and the system operates in the strong coupling regime at 20 dBm. The detuning not only reduces g but increases the required RF power to achieve $C = 1$. In practice, the generated sideband can compromise the output signal purity. In our case, using optical modes with different polarizations enables the separation of different polarizations with high extinction ratio (>20 dB) using a PBS (see Supplementary Note 8). On the other hand, it is worth noting that the same device can work as a non-reciprocal frequency shifter and polarization rotator with 100% conversion achievable for strongly overcoupled devices (that is, $\kappa_{ex} \approx \kappa$). It could serve as a key building block in photonic quantum computing[59].

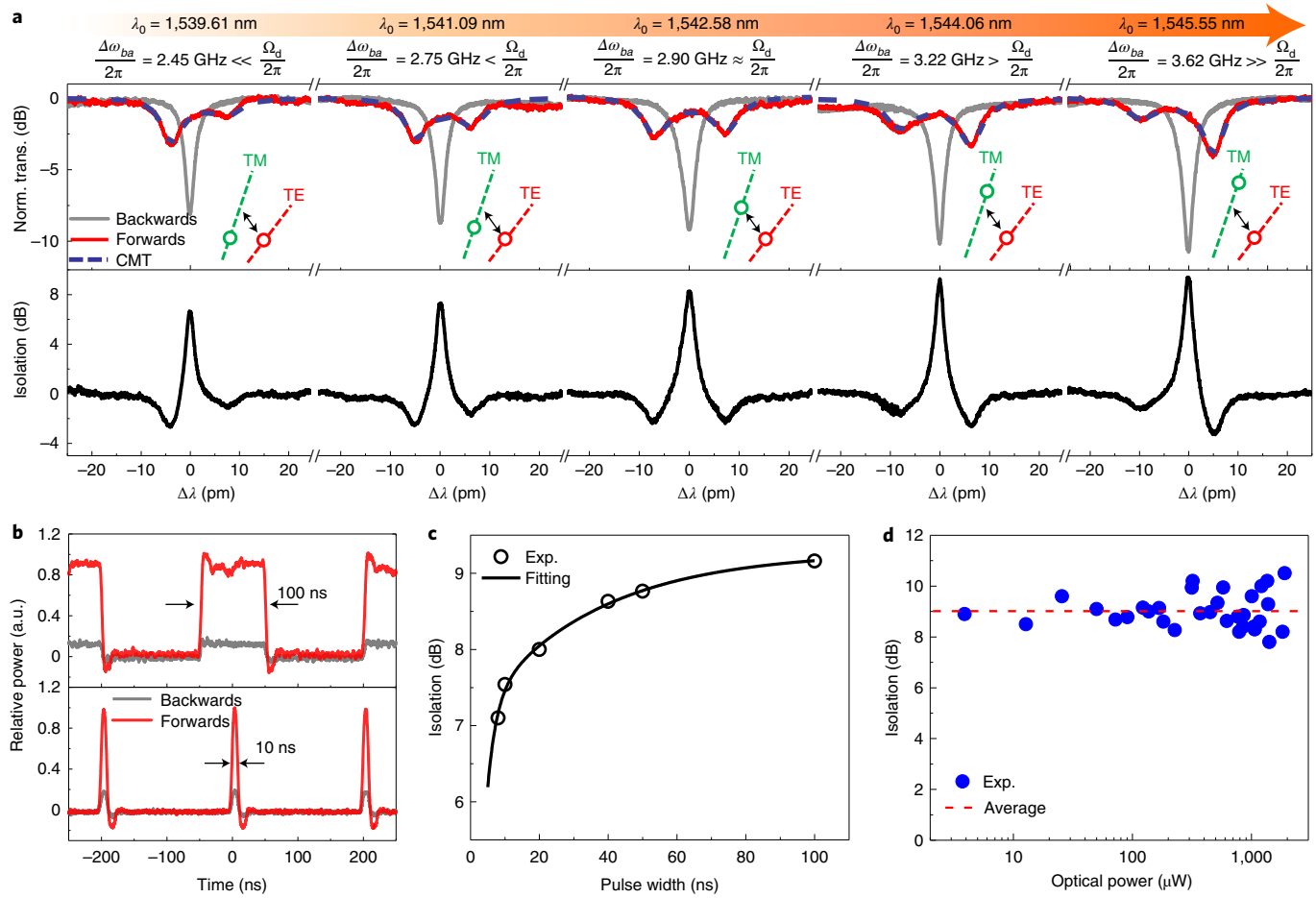

Fig. 5 | Influence of optical mode spacing, time-domain response and optical power linearity. a, Top panel: optical transmission spectra in the forward and backward directions, with increasing centre wavelength (left to right); $\Delta\omega_{ba}$ changes correspondingly due to the different FSRs of the TE_{00} and TM_{00} modes. Insets show the relative positions of the two modes in the $\omega - k$ space (not to scale). Bottom panel: spectra of isolation ratios varying with the centre wavelength. **b**, Transmission of optical pulse trains in the forward and backward directions for 100 ns and 10 ns pulse widths. The power is normalized to the maximum power of the forward pulse in each case. **c**, The isolation ratio decreases with narrower pulse widths due to the finite photon lifetime (~1.5 ns) in the optical cavity. Experimental data are fitted with an exponential function. **d**, Measured data showing that the isolation remains nearly constant around 9 dB over 30 dB dynamic range of the optical input power.

Detuning of optical mode spacing. As there is 380 MHz difference in FSR between the TE_{00} and TM_{00} modes (see Supplementary Note 2), their $\Delta\omega_{ba}$ varies from pair to pair for different centre wavelengths. Here, the dependence of isolation performance on $\Delta\omega_{ba}$ is studied in Fig. 5a under 20 dBm RF power. At $\lambda_0 = 1{,}542.58$ nm, $\Delta\omega_{ba}$ is nearly equal to the driving frequency Ω_d and the mode splitting is symmetric. As the optical resonance linewidths are around the gigahertz level, TE_{00} and TM_{00} modes can still be coupled even with a frequency mismatch between $\Delta\omega_{ba}/2\pi$ and $\Omega_d/2\pi$ on the order of 0.5 GHz. The mismatch leads to asymmetric mode splitting. Nevertheless, there is no prominent degradation of isolation within the measured range. The decrease of maximum isolation for shorter wavelength is caused by the reduction of extinction in the backward direction. This is because that shorter wavelength has smaller mode size and thus a weaker bus–microring external coupling rate κ_{ex} that leads to undercoupling. A maximum of 9.5 dB isolation is achieved at 1,545.55 nm, which is even larger than the matched symmetric case due to its better critical coupling. The isolator can therefore work simultaneously for multiple centre wavelengths, which is important for optical communication using wavelength multiplexing[60]. The wavelength range can be extended to cover the optical C-band by using pulley coupling scheme[61] to maintain critical coupling or slight overcoupling, and engineering the waveguide geometry to reach precise FSR match. On the other hand, thermal tuning to continuously shift the operating resonance can further increase the bandwidth.

Isolation of optical pulses. We further evaluate the optical isolator to demonstrate a unidirectional transmission of an optical pulse train to mimic (0, 1) data stream, as shown in Fig. 5b. The 100 ns pulse shows the quasi-static response, where the backward reflection is only 11% of the forward transmission. The bump at the pulse edge is caused by the limited bandwidth (~125 MHz) of the photodetector. The dynamic response is tested with 10 ns pulses, illustrating a vast contrast in the two directions. The isolation bandwidth can be inferred from the increasing isolation with increasing pulse duration, as revealed in Fig. 5c. A pulse of minimum 8 ns duration is measured, limited by the photodetector's bandwidth. Over 8 dB isolation is maintained for pulses longer than 20 ns; however, the isolation drops exponentially when the pulse duration is shorter than 20 ns, which is ultimately limited by the photon lifetime of ~1.5 ns, corresponding to 680 MHz linewidth of the optical resonance.

Optical power linearity. Dynamic reciprocity has been a well-known limitation for most optical isolators relying on optical nonlinearity, where the isolation degrades dramatically when light transmits

Table 1 | Comparison of monolithically integrated, magnetic-free optical isolator devices

Year	Scheme	Structure	Material	Isolation	Insertion loss	Bandwidth	Power
2020[37]	Nonlinear optics	Ring	Si	20 dB	1.3 dB	20 GHz	No drive
2014[29]	Synthetic magnetic	MZI	Doped Si	2.4 dB	N/A	20 nm	34 dBm
2021[30]	Synthetic magnetic	Ring	AlN	3 dB	9 dB	4 GHz	16 dBm
2021[31]	Synthetic magnetic	Ring	Doped Si	13 dB	1 dB	2 GHz	−3 dBm
2012[50]	Spatio-temporal	MZI	Doped Si	3 dB	70 dB	200 GHz	25 dBm
2018[53]	Spatio-temporal	MZI	Si	39 dB[a]	N/A	125 GHz	90 mW[b]
2018[54]	Spatio-temporal	Ring	AlN	15 dB[a]	N/A	1 GHz	18 dBm
2021[55]	Spatio-temporal	MZI	Si + AlN	16 dB[a]	N/A	100 GHz	21 dBm
This work	Spatio-temporal	Ring	Si_3N_4 + AlN	10 dB	0.1–1 dB	0.7 GHz	25 dBm

[a]The isolation is the non-reciprocal response of modulation sideband. [b]Optical drive power, whereas others are electrical power.

simultaneously in both directions and the optical power exceeds a certain threshold[37,48]. In our work, with only electrical drives, the optical linearity is preserved as long as the intracavity photon number is smaller than the phonon number. As the phonon frequency is five orders of magnitude smaller than the photon frequency, theoretically it suggests maximum of 6 kW optical power for 20 dBm RF power in the experiment; however, the optical linearity of our isolator is eventually limited to several watts due to the Kerr nonlinearity of Si_3N_4. The quasi-square waveguide cross-section used here has a normal group velocity dispersion and the optical microresonator has low optical $Q < 5 \times 10^5$, which suppress Kerr parametric oscillation[16]. The linearity is experimentally verified in microwatt to milliwatt range, as shown in Fig. 5d. The optical isolation remains nearly constant within the measured range. The large variation at high optical power is mainly due to the optical thermal nonlinearity as the laser is swept across the optical resonance. Theoretically there is no limit on the lower bound of the optical power, thus our device can work for photonic quantum computing[59].

Discussion

We have demonstrated an integrated optical isolator by spatio-temporal modulation of a Si_3N_4 microring resonator via three AlN piezoelectric actuators. The device has been fully characterized in terms of RF phases, RF powers, optical spectra and optical powers, showing agreement with theoretical models and numerical simulations. Table 1 summarizes recently demonstrated integrated, magnetic-free isolators (to the best of our knowledge), including our work. A comprehensive comparison with other experimental realizations is found in Supplementary Note 10.

Although promising progresses have been made using nonlinear optics[37] and synthetic magnetic field[30,31], most spatio-temporal modulation demonstrations[53–55] are still in the non-reciprocal sideband modulation regime. In this work, the HBAR AOM helps to boost the optical cooperativity C beyond unity and enter strong coupling regime, thanks to the power handling capability and the tight acoustic confinement of our devices. We obtain 10 dB isolation with 300 mW total RF power applied on three actuators. Notably, a record-low insertion loss of 0.1 dB is achieved due to the intrinsic low loss of Si_3N_4 waveguides. In contrast to the scheme relying on nonlinear optics, the electrical drive used in our work largely preserves the optical linearity by separating RF driving and optical sensing in two different domains.

In the future, the isolation can be improved by optimizing the bus–microring coupling gap to reach perfect critical coupling or slight overcoupling. Furthermore, it has been demonstrated recently that perfect critical coupling in an initially overcoupled device can be achieved with a controllable manner[62]. Using an overcoupled device with 600 nm coupling gap, we achieve 41 dB isolation and 1.9 dB insertion loss under 2 W total RF power (see Supplementary Note 9). The RF power consumption can be reduced to a few milliwatts by using microresonators of smaller radii to increase the piezo-optomechanical coupling efficiency[63], and scandium-doped AlN to increase the piezoelectric coefficient[64] (see Supplementary Note 11). With these improvements, our electrically driven, magnetic-free optical isolators could be reliably incorporated as a key building block into current integrated opto-electronic systems.

Online content

Any methods, additional references, Nature Research reporting summaries, source data, extended data, supplementary information, acknowledgements, peer review information; details of author contributions and competing interests; and statements of data and code availability are available at https://doi.org/10.1038/s41566-021-00882-z.

Received: 8 April 2021; Accepted: 18 August 2021;
Published online: 21 October 2021

References

1. Xiang, C. et al. Narrow-linewidth III–V/Si/Si_3N_4 laser using multilayer heterogeneous integration. *Optica* **7**, 20–21 (2020).
2. Xiang, C. et al. Laser soliton microcombs heterogeneously integrated on silicon. *Science* **373**, 99–103 (2021).
3. Wang, C. et al. Integrated lithium niobate electro-optic modulators operating at CMOS-compatible voltages. *Nature* **562**, 101–104 (2018).
4. He, M. et al. High-performance hybrid silicon and lithium niobate Mach–Zehnder modulators for 100 gbit s^{-1} and beyond. *Nat. Photon.***13**, 359–364 (2019).
5. Tian, H. et al. Hybrid integrated photonics using bulk acoustic resonators. *Nat. Commun.* **11**, 3073 (2020).
6. Liu, J. et al. Monolithic piezoelectric control of soliton microcombs. *Nature* **583**, 385–390 (2020).
7. Tadesse, S. A. & Li, M. Sub-optical wavelength acoustic wave modulation of integrated photonic resonators at microwave frequencies. *Nat. Commun.* **5**, 5402 (2014).
8. Shao, L. et al. Microwave-to-optical conversion using lithium niobate thin-film acoustic resonators. *Optica* **6**, 1498–1505 (2019).
9. Zhang, M., Wang, C., Cheng, R., Shams-Ansari, A. & Lončar, M. Monolithic ultra-high-q lithium niobate microring resonator. *Optica* **4**, 1536–1537 (2017).
10. Chang, L. et al. Ultra-efficient frequency comb generation in algaas-on-insulator microresonators. *Nat. Commun.* **11**, 1331 (2020).
11. Xuan, Y. et al. High-q silicon nitride microresonators exhibiting low-power frequency comb initiation. *Optica* **3**, 1171–1180 (2016).
12. Ji, X. et al. Ultra-low-loss on-chip resonators with sub-milliwatt parametric oscillation threshold. *Optica* **4**, 619–624 (2017).
13. Liu, J. et al. High-yield, wafer-scale fabrication of ultralow-loss, dispersion-engineered silicon nitride photonic circuits. *Nat. Commun.* **12**, 2236 (2021).
14. Moss, D. J., Morandotti, R., Gaeta, A. L. & Lipson, M. New CMOS-compatible platforms based on silicon nitride and hydex for nonlinear optics. *Nat. Photon.* **7**, 597–607 (2013).

15. Gaeta, A. L., Lipson, M. & Kippenberg, T. J. Photonic-chip-based frequency combs. *Nat. Photon.* **13**, 158–169 (2019).
16. Kippenberg, T. J., Gaeta, A. L., Lipson, M. & Gorodetsky, M. L. Dissipative Kerr solitons in optical microresonators. *Science* **361**, eaan8083 (2018).
17. Wang, C. et al. Monolithic lithium niobate photonic circuits for Kerr frequency comb generation and modulation. *Nat. Commun.* **10**, 978 (2019).
18. He, Y. et al. Self-starting bi-chromatic $LiNbO_3$ soliton microcomb. *Optica* **6**, 1138–1144 (2019).
19. Jung, H., Xiong, C., Fong, K. Y., Zhang, X. & Tang, H. X. Optical frequency comb generation from aluminum nitride microring resonator. *Opt. Lett.* **38**, 2810–2813 (2013).
20. Liu, X. et al. Integrated high-q crystalline aln microresonators for broadband kerr and raman frequency combs. *ACS Photon.* **5**, 1943–1950 (2018).
21. Pu, M., Ottaviano, L., Semenova, E. & Yvind, K. Efficient frequency comb generation in AlGaAs-on-insulator. *Optica* **3**, 823–826 (2016).
22. Jin, W. et al. Hertz-linewidth semiconductor lasers using cmos-ready ultra-high-*Q* microresonators. *Nat. Photon* **15**, 346–353 (2021).
23. Srinivasan, K. & Stadler, B. J. H. Magneto-optical materials and designs for integrated TE- and TM-mode planar waveguide isolators: a review [invited]. *Opt. Mater. Express* **8**, 3307–3318 (2018).
24. Bi, L. et al. On-chip optical isolation in monolithically integrated non-reciprocal optical resonators. *Nat. Photon.* **5**, 758–762 (2011).
25. Huang, D. et al. Electrically driven and thermally tunable integrated optical isolators for silicon photonics. *IEEE J. Sel. Top. Quantum Electron.* **22**, 271–278 (2016).
26. Yan, W. et al. Waveguide-integrated high-performance magneto-optical isolators and circulators on silicon nitride platforms. *Optica* **7**, 1555–1562 (2020).
27. Awschalom, D. et al. Development of quantum interconnects (QuICs) for next-generation information technologies. *PRX Quantum* **2**, 017002 (2021).
28. Fang, K., Yu, Z. & Fan, S. Realizing effective magnetic field for photons by controlling the phase of dynamic modulation. *Nat. Photon.* **6**, 782–787 (2012).
29. Tzuang, L. D., Fang, K., Nussenzveig, P., Fan, S. & Lipson, M. Non-reciprocal phase shift induced by an effective magnetic flux for light. *Nat. Photon.* **8**, 701–705 (2014).
30. Kim, S., Sohn, D. B., Peterson, C. W. & Bahl, G. On-chip optical non-reciprocity through a synthetic hall effect for photons. *APL Photon.* **6**, 011301 (2021).
31. Dostart, N., Gevorgyan, H., Onural, D. & Popović, M. A. Optical isolation using microring modulators. *Opt. Lett.* **46**, 460–463 (2021).
32. Fan, L. et al. An all-silicon passive optical diode. *Science* **335**, 447–450 (2012).
33. Peng, B. et al. Parity–time-symmetric whispering-gallery microcavities. *Nat. Phys.* **10**, 394–398 (2014).
34. Chang, L. et al. Parity–time symmetry and variable optical isolation in active–passive-coupled microresonators. *Nat. Photon.* **8**, 524–529 (2014).
35. Bino, L. D. et al. Microresonator isolators and circulators based on the intrinsic nonreciprocity of the Kerr effect. *Optica* **5**, 279–282 (2018).
36. Hua, S. et al. Demonstration of a chip-based optical isolator with parametric amplification. *Nat. Commun.* **7**, 13657 (2016).
37. Yang, K. Y. et al. Inverse-designed non-reciprocal pulse router for chip-based LiDAR. *Nat. Photon.* **14**, 369–374 (2020).
38. Cao, Q.-T. et al. Reconfigurable symmetry-broken laser in a symmetric microcavity. *Nat. Commun.* **11**, 1136 (2020).
39. Shen, Z. et al. Experimental realization of optomechanically induced non-reciprocity. *Nat. Photon.* **10**, 657–661 (2016).
40. Ruesink, F., Miri, M.-A., Alù, A. & Verhagen, E. Nonreciprocity and magnetic-free isolation based on optomechanical interactions. *Nat. Commun.* **7**, 13662 (2016).
41. Shen, Z. et al. Reconfigurable optomechanical circulator and directional amplifier. *Nat. Commun.* **9**, 1797 (2018).
42. Ruesink, F., Mathew, J. P., Miri, M.-A., Alù, A. & Verhagen, E. Optical circulation in a multimode optomechanical resonator. *Nat. Commun.* **9**, 1798 (2018).
43. Kang, M. S., Butsch, A. & Russell, P. S. J. Reconfigurable light-driven opto-acoustic isolators in photonic crystal fibre. *Nat. Photon.* **5**, 549–553 (2011).
44. Poulton, C. G. et al. Design for broadband on-chip isolator using stimulated Brillouin scattering in dispersion-engineered chalcogenide waveguides. *Opt. Express* **20**, 21235–21246 (2012).
45. Dong, C.-H. et al. Brillouin-scattering-induced transparency and non-reciprocal light storage. *Nat. Commun.* **6**, 6193 (2015).
46. Kim, J., Kuzyk, M. C., Han, K., Wang, H. & Bahl, G. Non-reciprocal Brillouin scattering induced transparency. *Nat. Phys.* **11**, 275–280 (2015).
47. Merklein, M. et al. On-chip broadband nonreciprocal light storage. *Nanophotonics* **10**, 75–82 (2021).
48. Shi, Y., Yu, Z. & Fan, S. Limitations of nonlinear optical isolators due to dynamic reciprocity. *Nat. Photon.* **9**, 388–392 (2015).
49. Yu, Z. & Fan, S. Complete optical isolation created by indirect interband photonic transitions. *Nat. Photon.* **3**, 91–94 (2009).
50. Lira, H., Yu, Z., Fan, S. & Lipson, M. Electrically driven nonreciprocity induced by interband photonic transition on a silicon chip. *Phys. Rev. Lett.* **109**, 033901 (2012).
51. Sounas, D. L. & Alù, A. Angular-momentum-biased nanorings to realize magnetic-free integrated optical isolation. *ACS Photon.* **1**, 198–204 (2014).
52. Shi, Y., Lin, Q., Minkov, M. & Fan, S. Nonreciprocal optical dissipation based on direction-dependent Rabi splitting. *IEEE J. Sel. Top. Quantum Electron.* **24**, 1–7 (2018).
53. Kittlaus, E. A., Otterstrom, N. T., Kharel, P., Gertler, S. & Rakich, P. T. Non-reciprocal interband Brillouin modulation. *Nat. Photon.* **12**, 613–619 (2018).
54. Sohn, D. B., Kim, S. & Bahl, G. Time-reversal symmetry breaking with acoustic pumping of nanophotonic circuits. *Nat. Photon.* **12**, 91–97 (2018).
55. Kittlaus, E. A. et al. Electrically driven acousto-optics and broadband non-reciprocity in silicon photonics. *Nat. Photon.* **15**, 43–52 (2021).
56. Fan, L. et al. Superconducting cavity electro-optics: a platform for coherent photon conversion between superconducting and photonic circuits. *Sci. Adv.* **4**, eaar4994 (2018).
57. Balram, K. C., Davanço, M., Lim, J. Y., Song, J. D. & Srinivasan, K. Moving boundary and photoelastic coupling in gaas optomechanical resonators. *Optica* **1**, 414–420 (2014).
58. Stanfield, P. R., Leenheer, A. J., Michael, C. P., Sims, R. & Eichenfield, M. CMOS-compatible, piezo-optomechanically tunable photonics for visible wavelengths and cryogenic temperatures. *Opt. Express* **27**, 28588–28605 (2019).
59. Lukens, J. M. & Lougovski, P. Frequency-encoded photonic qubits for scalable quantum information processing. *Optica* **4**, 8–16 (2017).
60. Marin-Palomo, P. et al. Microresonator-based solitons for massively parallel coherent optical communications. *Nature* **546**, 274 (2017).
61. Moille, G. et al. Broadband resonator-waveguide coupling for efficient extraction of octave-spanning microcombs. *Opt. Lett.* **44**, 4737–4740 (2019).
62. Sohn, D., Örsel, O. E. & Bahl, G. Electrically driven linear optical isolation through phonon mediated autler-townes splitting. Preprint at https://arxiv.org/abs/2104.04803 (2021).
63. Blésin, T., Tian, H., Bhave, S. & Kippenberg, T. Quantum coherent microwave-optical transduction using high overtone bulk acoustic resonances. Preprint at https://arxiv.org/abs/2103.00471 (2021).
64. Pirro, M. et al. Characterization of dielectric and piezoelectric properties of ferroelectric alscn thin films. In *2021 IEEE 34th International Conference on Micro Electro Mechanical Systems (MEMS)* 646–649 (IEEE, 2021).

Methods

Device fabrication. The Si_3N_4 PIC is fabricated using the photonic Damascene process[13]. The monolithic integration of piezoelectric AlN actuators on top of Si_3N_4 microresonators is illustrated in ref. [5,6]. Films of 100 nm Mo and 1 μm AlN are sputtered on the wafer through foundry services (Plasma-Therm). The actuators are patterned by thick photoresist SPR220-4.5 and dry-etched using Cl_2 and BCl_3 in Panasonic E620 Etcher. The bottom molybdenum electrodes are patterned by photoresist AZ1518 and dry-etched using Cl_2 in the same etcher. Finally, the top 100 nm aluminium is deposited by an electron-beam evaporator and patterned using a standard lift-off process. The SiO_2 release process is shown in Fig. 1d. The centre release hole is patterned using photolithography, and SiO_2 is dry-etched to expose the silicon substrate. The silicon is then isotropically etched using the SF_6 Bosch process to undercut and suspend the SiO_2 membrane.

Design of Si_3N_4 waveguides for phase matching. From the microring's resonant condition $k=2\pi/\lambda=m/R$, the momentum is related to the azimuthal order m of the mode and the microring's radius R. As the three actuators cover the entire microring, the generated rotating acoustic wave has an effective wavelength of $2\pi R$, and thus the azimuthal order is $m_c=1$. The phase matching condition thus requires the azimuthal order difference $\Delta m_{ab}=m_a-m_b=m_c=1$ between the TE_{00} and TM_{00} modes. As the Si_3N_4 waveguide is fully cladded with SiO_2, a quasi-square waveguide cross-section ($810\times820\,nm^2$), as shown in Fig. 2b inset, is designed to have slightly different effective refractive indices for the two optical modes (see Supplementary Note 1). Here, phase matching requires the two optical modes to co-propagate, with the counter-propagating acoustic wave. In the final devices used in the experiment, the azimuthal order difference is measured and calibrated (see Supplementary Note 2) to be around $\Delta m_{ab}=4$. Due to the discrete nature of the spatial modulation, there are higher-azimuthal-order Fourier components simultaneously excited that can fulfil phase matching at the expense of lower efficiency[51].

Measurement set-up. The electromechanical S_{11} is measured by detecting the reflected microwave signal using a vector network analyser (VNA, Agilent E8364B), where the electrical signal is applied to the device through an RF GSG probe (Cascade ACP40-GSG-150). To measure the optomechanical S_{21}, continuous-wave (CW) light from a diode laser (Velocity Tunable Laser 6328) is edge-coupled into the chip using a lensed fibre and an inverse taper with around 50 μW power on chip. An RF signal of −5 dBm power is applied from the port 1 of the VNA to drive the AlN actuator. The light intensity modulation is detected by a 12 GHz photodiode (New Focus 1544), whose output is sent back to port 2 of the network analyser.

In the main optical isolation measurement, three RF signal generators (Agilent E8257D) output RF drives that are amplified by three RF amplifiers (ZHL-5W-63-S+) before going into the device. The relative phases are controlled by their built-in phase controllers after synchronization by their internal 10 MHz clock. The CW laser's wavelength is continuously swept across the optical resonance. The input light polarization is controlled by fibre polarization controllers (FPC561). The light input direction is selected by a microelectromechanical system (MEMS) 2×2 optical switch (OSW22-1310E). The output TE and TM polarizations are separated by a fibre PBS (PBC1550SM-FC), and are measured by two photodetectors (New Focus 1811), the signals of which are recorded by an oscilloscope (MSO8104A). The non-reciprocal transmission is found in Supplementary Video 1. Note that the optical axis of the PBS is fixed and thus a polarization controller is needed to align the TE and TM polarizations with respect to the optical axis of the PBS. During the measurement, TE polarization is selected by rotating the polarization controller until that only TE mode resonances are observed. This process is repeated for both directions. It is worth noting that, although the polarization will change as we switch the MEMS optical switch, the polarization right before the PBS will be the same, since the optical switch itself is a reciprocal device. During the experiments, the RF phases are actively adjusted to compensate the drift of RF phases due to the thermal heating and HBAR resonance shift. The RF phases are calibrated by comparing the transmission spectrum with numerical simualtions.

For measuring isolation of optical pulses, the input light before the optical switch is modulated by an electro-optic intensity modulator (Lucent 2623CSA), and the input pulse is generated by a function generator (Agilent 33250A). The 100 ns (10 ns) pulse has a repetition rate of 4 MHz (5 MHz). Supplementary Video 2 shows the experimental demonstration. To measure the optical linearity, an erbium-doped fibre amplifier (EDFA-I-B) is used before the optical switch to increase the optical power to above 100 μW.

Derivation of coupled mode equations. The three-wave mixing process (two optical modes $\hat{a}$ and $\hat{b}$, and one mechanical mode $\hat{c}$) can be described by the quantum interaction Hamiltonian:

$$\hat{H}_I = \hbar g_0(\hat{a}\hat{b}^\dagger\hat{c} + \hat{a}^\dagger\hat{b}\hat{c}^\dagger) \tag{5}$$

assuming that phase matching is fulfilled and $\hat{a}$ has a smaller frequency than $\hat{b}$. Under these conditions, the optomechanical interaction can be understood as the combination of two processes: (1) $\hat{a}\hat{b}^\dagger\hat{c}$, annihilation of a photon $\hat{a}$ and a phonon $\hat{c}$ and generation of one higher-frequency photon $\hat{b}$; (2) $\hat{a}^\dagger\hat{b}\hat{c}^\dagger$, annihilation of one photon $\hat{b}$ and generation of a photon $\hat{a}$ and a phonon $\hat{c}$. Following an approach similar to ref. [56], the equations of motion for the average of the annihilation operators can be obtained by assuming resolved sidebands and rotating-wave approximation:

$$\frac{d}{dt}\langle\hat{a}\rangle = -(i\Delta_a + \frac{\kappa_a}{2})\langle\hat{a}\rangle - ig_0\left\langle\hat{b}\right\rangle\left\langle\hat{c}^\dagger\right\rangle + \sqrt{\kappa_{a,\mathrm{ex}}}\langle\hat{a}_{\mathrm{in}}\rangle \tag{6}$$

$$\frac{d}{dt}\left\langle\hat{b}\right\rangle = -(i\Delta_b + \frac{\kappa_b}{2})\left\langle\hat{b}\right\rangle - ig_0\langle\hat{a}\rangle\langle\hat{c}\rangle \tag{7}$$

$$\frac{d}{dt}\langle\hat{c}\rangle = -(i\Omega_{\mathrm{m}} + \frac{\Gamma_c}{2})\langle\hat{c}\rangle - ig_0\left\langle\hat{a}^\dagger\right\rangle\left\langle\hat{b}\right\rangle + \sqrt{\Gamma_{c,\mathrm{ex}}}\langle\hat{c}_{\mathrm{in}}\rangle e^{-i\Omega_d t} \tag{8}$$

$$\langle\hat{a}_{\mathrm{out}}\rangle = \langle\hat{a}_{\mathrm{in}}\rangle - \sqrt{\kappa_{a,\mathrm{ex}}}\langle\hat{a}\rangle \tag{9}$$

$$\left\langle\hat{b}_{\mathrm{out}}\right\rangle = -\sqrt{\kappa_{b,\mathrm{ex}}}\left\langle\hat{b}\right\rangle \tag{10}$$

where $\Gamma_c/2\pi$ and $\Gamma_{c,\mathrm{ex}}/2\pi$ are the total loss rate (11 MHz) of the mechanical mode and the external coupling rate (22 kHz) from the microwave channel to the HBAR phonons, and $|\langle\hat{c}_{\mathrm{in}}\rangle| = \sqrt{P_{\mathrm{in}}/\hbar\Omega_d}$ is the input microwave amplitude, where P_{in} is the input RF power[63]. Assuming that the optomechanical coupling (term $g_0\left\langle\hat{a}^\dagger\right\rangle\left\langle\hat{b}\right\rangle$ in equation (8)) has a much smaller contribution than the microwave drive, the mean intracavity amplitude of $\bar{c}$ at steady state is:

$$\bar{c} = \sqrt{\bar{n}_c}e^{-i\Omega_d t} \tag{11}$$

$$\bar{n}_c = \frac{\Gamma_{c,\mathrm{ex}}}{(\Omega_d-\Omega_m)^2+\Gamma_c^2/4}\frac{P_{\mathrm{in}}}{\hbar\Omega_d} \tag{12}$$

By inserting equation (11) into equations (6) and (7), we obtain equations (1) and (2) in the main text. Due to the modulation, the frequency of mode $\hat{b}$ is shifted by Ω_d in the rotating frame of ω_L. The slow amplitude and fast oscillation of mode $\hat{b}$ can be separated by substituting $\hat{b}$ with $\tilde{b}e^{-i\Omega_d t}$. At steady state, equations (1) and (2) can be solved by setting time derivatives to zero, and after some linear algebra[56] we obtain the general expressions for transmission T and sideband conversion efficiency η:

$$T = \left|\frac{\langle\hat{a}_{\mathrm{out}}\rangle}{\langle\hat{a}_{\mathrm{in}}\rangle}\right|^2 = \left|1 - \frac{\kappa_{a,\mathrm{ex}}}{i\Delta_a + \frac{\kappa_a}{2} + \frac{g^2}{i(\Delta_b-\Omega_d)+\frac{\kappa_b}{2}}}\right|^2 \tag{13}$$

$$\eta = \left|\frac{\left\langle\hat{b}_{\mathrm{out}}\right\rangle}{\langle\hat{a}_{\mathrm{in}}\rangle}\right|^2 = \frac{\kappa_{a,\mathrm{ex}}}{\kappa_a}\frac{\kappa_{b,\mathrm{ex}}}{\kappa_b}\frac{4C}{|C+(1+\frac{2i\Delta_a}{\kappa_a})(1+\frac{2i(\Delta_b-\Omega_d)}{\kappa_b})|^2} \tag{14}$$

where $\Delta_b-\Omega_d=\Delta_{ba}+\Delta_a-\Omega_d$. C is the photon–photon cooperativity as mentioned in the main text. It can be seen that when $\Delta_a=0$ and $\Delta_{ba}=\Omega_d$, equations (13) and (14) reduce to equations (3) and (4). Equations (13) and (14) are used for data fitting in Figs. 4 and 5. The mode splitting can be found from equation (13), assuming $\Delta_a \gg \kappa_a, \kappa_b$ and $\Delta_{ba}=\Omega_d$:

$$T \approx \left|1 - \frac{(i\Delta_a + \frac{\kappa_b}{2})\kappa_{a,\mathrm{ex}}}{(g+\Delta_a)(g-\Delta_a) + i(\frac{\kappa_a+\kappa_b}{2})\Delta_a}\right|^2 \tag{15}$$

where the transmission minimum is reached when $\Delta_a=\pm g$. Thus the mode splitting is $2g$.

Data availability

The code and data used to produce the plots within this work are available on Zenodo (https://doi.org/10.5281/zenodo.5120854). All other data used in this study are available from the corresponding authors on reasonable request.

Acknowledgements

This work was supported by US National Science Foundation's RAISE TAQS program under grant no. PHY 18-39164, by NSF QISE-Net under grant no. DMR 17-47426, by the Air Force Office of Scientific Research under award no. FA8655-20-1-7009, by funding from the EU H2020 research and innovation programme under grant agreement no. 732894 (HOT), and by Swiss National Science Foundation under grant agreement no. 176563 (BRIDGE). Samples were fabricated in the EPFL center of MicroNanoTechnology (CMi), and Birck Nanotechnology Center at Purdue University. AlN deposition was performed at Plasma-Therm LLC. We thank Y. Shi for valuable discussions.

Author contributions

H.T. and J.L. designed the devices. J.L., H.T. and R.N.W. developed the process and fabricated the samples, with the assistance from J.H.. H.T. performed the experiment and simulations, and analysed the data. A.S. performed the experiment on the overcoupled device with the assistance from T.B.. H.T. and J.L. wrote the manuscript, with input from others. S.A.B and T.J.K supervised the collaboration.

Competing interests

The authors declare no competing interests.

Additional information

Supplementary information The online version contains supplementary material available at https://doi.org/10.1038/s41566-021-00882-z.

Correspondence and requests for materials should be addressed to Tobias J. Kippenberg or Sunil A. Bhave.

Peer review information *Nature Photonics* thanks Chun-Hua Dong and the other, anonymous, reviewer(s) for their contribution to the peer review of this work.

Reprints and permissions information is available at www.nature.com/reprints.

nature portfolio

https://doi.org/10.1038/s41566-021-00882-z

Supplementary information

Magnetic-free silicon nitride integrated optical isolator

In the format provided by the authors and unedited

Supplementary Information to: Magnetic-Free Silicon Nitride Integrated Optical Isolator

Hao Tian[1,*], Junqiu Liu[2,*], Anat Siddharth[2], Rui Ning Wang[2], Terence Blésin[2], Jijun He[2], Tobias J. Kippenberg[2,†], Sunil A. Bhave[1,†]

[1] *OxideMEMS Lab, Purdue University, 47907 West Lafayette, IN, USA*

[2] *Institute of Physics, Swiss Federal Institute of Technology Lausanne (EPFL), 1015 Lausanne, Switzerland*

∗ *These authors contributed equally to this work.*

† *E-mail: tobias.kippenberg@epfl.ch, bhave@purdue.edu*

Supplementary Note 1: Design of quasi-square optical waveguide

As mentioned in the main text, phase matching is key for efficient mode coupling. This requires that the two optical modes have the frequency difference matching the mechanical frequency (below 5 GHz), and the azimuthal order difference equals to the effective azimuthal order of the modulation wave. Satisfying the frequency requirement is relatively easy since at the mode anti-crossing the two modes are closely spaced. It is more stringent for momentum. Since the three actuators cover the entire microring, the effective wavelength of the modulation wave is $2\pi R$ indicating that the azimuthal order is 1. This requires the two optical modes to have very close effective refractive indices. In the case of fully SiO_2-cladded Si_3N_4, an intuitive way is to design a quasi-square waveguide cross-section where the difference of effective refractive indices between TE_{00} and TM_{00} modes is determined by the aspect ratio of the waveguide's height h and width w_b, as shown in Supplementary Fig. 1a. The sidewall angle θ is also included in the design based on previous experiments[1–3]. As h depends on thin-film deposition and chemical-mechanical polishing, w_b depends on photolithography, and θ depends on reactive ion etching (RIE), they all show variations over wafer scale due to fabrication, which should be taken into account in the waveguide design.

For specific waveguide geometry (h, w_b, and θ), the resonant frequency and azimuthal order of the two modes are simulated using Finite Element Method (with COMSOL), where the frequency and azimuthal order difference $\Delta m = m_\mathrm{TE} - m_\mathrm{TM}$ can be calculated. For fixed choice of θ and Δm, there is a combination of h and w_b that will generate mode anti-crossing around 1550 nm wavelength (193.5 THz frequency), as seen in Supplementary Fig. 1c. The initial design targets at $\Delta m = 1$ with sidewall angle $\theta = 89°$ (red line with red filled square). As the waveguide height varies between 800 to 820 nm across the wafer, the waveguide width is designed to vary from 810 to 830 nm to take into account the height variations. The width is designed to be slightly larger than the height such that TE_{00} has a higher effective refractive index than that of TM_{00}, and thus a slightly higher azimuthal order. To maintain Δm, the width and height need to increase (or decrease) together to keep the aspect ratio. As the sidewall angle decreases to $88°$, the required height increases at the same width (red line with red unfilled square). Nevertheless, the curve still crosses the height variation (blue shaded area) at small width. In this case, the initial design is supposed to cover the variation of height, width and sidewall angle.

Supplementary Note 2: Calibration of azimuthal order difference Δm

In this section, the azimuthal order difference Δm of the fabricated device is calibrated, showing deviation from the initial design in the previous section. The waveguide cross-section is shown in the SEM in Supplementary Fig. 1b. The sidewall angles deviate from $89°$ with the smallest angle being $83°$, which will be corrected in the following analysis. For the device shown in the main text, the spectra of TE_{00} and TM_{00} mode pairs are measured over a broad wavelength range, as shown in Supplementary Fig. 1d. A mode anti-crossing is found around 1540 nm. At longer wavelength, TE

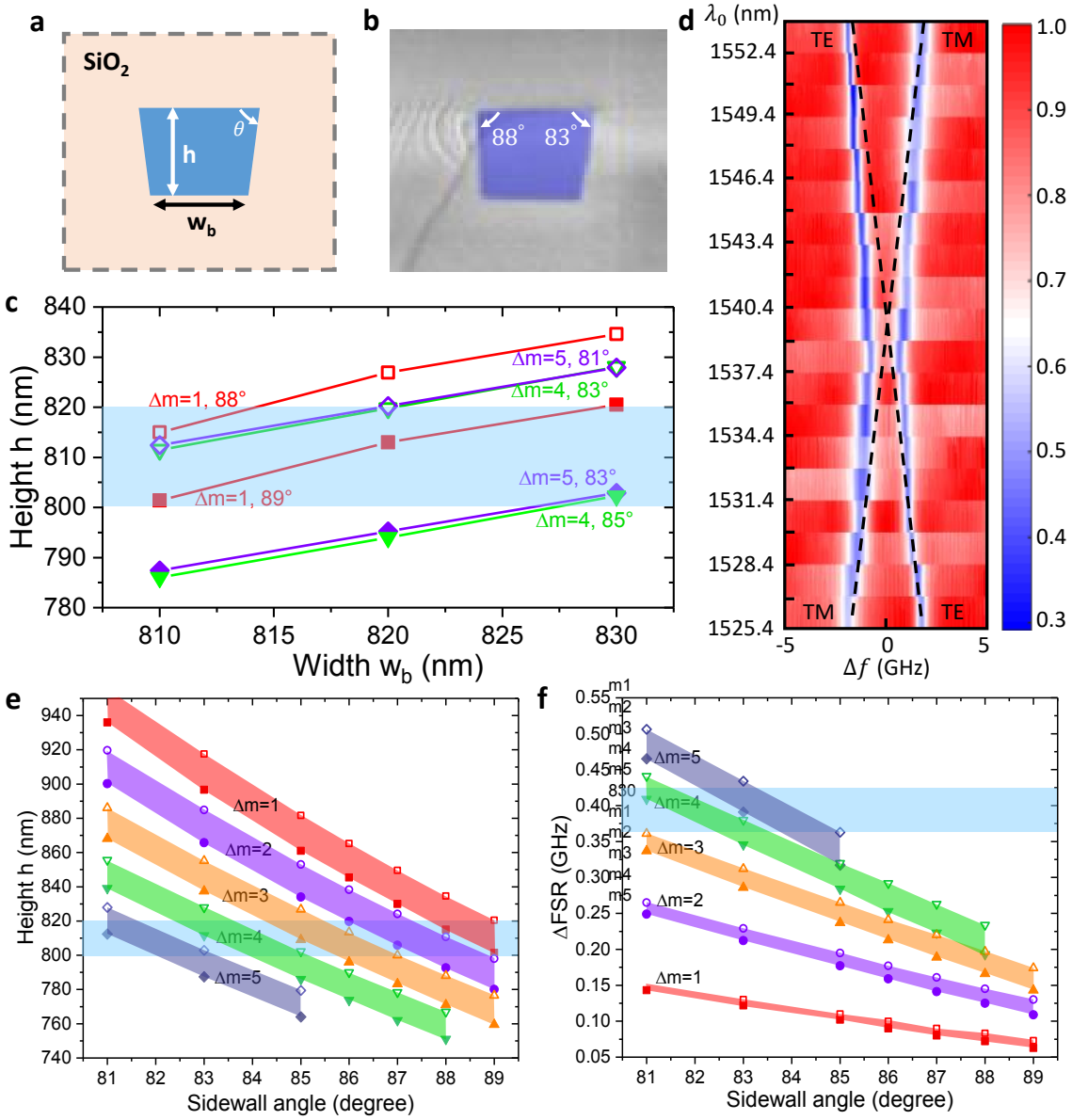

Supplementary Figure 1: Optical waveguide design and calibration of azimuthal order difference Δm. **a** Schematic of optical waveguide cross-section with Si_3N_4 (blue) fully embedded in isotropic SiO_2 cladding. The definition of height h, bottom width w_b, and sidewall angle θ are as labeled. **b** False colored SEM showing the cross-section of the fabricated optical waveguide. The sidewall angles are as labeled. **c** Simulations suggests that the required h and w_b combination produces close TE_{00} and TM_{00} modes around 1550 nm with $\Delta m = 1$ (red), $\Delta m = 4$ (green), $\Delta m = 5$ (purple). Different sidewall angles are studied and labeled. The blue shaded area indicates the variation of waveguide height in the fabrication. **d** Measured TE_{00} and TM_{00} mode anti-crossing around 1540 nm. The wavelength λ_0 is the center wavelength between TE_{00} and TM_{00}. **e** Simulated height h that generates close TE_{00} and TM_{00} modes, and **f** corresponding FSR difference ΔFSR for different sidewall angles and Δm. The variation of width w_b is included as lower (810 nm) and higher (830 nm) bounds of each Δm plot. The blue shaded areas are experimental variations.

mode has lower frequency than the TM mode ($f_{\mathrm{TE}} < f_{\mathrm{TM}}$), while at shorter wavelength $f_{\mathrm{TE}} > f_{\mathrm{TM}}$. This shows that TE mode has a larger FSR than the TM mode, i.e. $\Delta\mathrm{FSR} = \mathrm{FSR}_{\mathrm{TE}} - \mathrm{FSR}_{\mathrm{TM}} \approx 380$ MHz. This FSR difference is used to find approximately the Δm of the measured device by comparing with numerical simulations (COMSOL), as illustrated in Supplementary Fig. 1f.

Supplementary Figure 1e shows the simulation of the required h as a function of sidewall angle θ for different Δm. The variation of width is also included in each Δm plot with the lower bound being $w_{\mathrm{b}} = 810$ nm and upper bound being $w_{\mathrm{b}} = 830$ nm. We find that, as the sidewall angle decreases, the required height increases, and it is higher for smaller Δm. For angle around 83°, the height achieved in the experiment overlaps with $\Delta m = 4 \sim 5$. In Supplementary Fig. 1f, the change of ΔFSR with sidewall angle is also plotted. It can be seen that ΔFSR is smaller for small Δm, which means that the two optical modes has closer refractive indices. ΔFSR also increases with decreasing sidewall angle. Based on the measured ΔFSR, $\Delta m = 4$ shows better overlap with both height and Δm. In the future, Δm can be precisely engineered to 1 with better estimation of the variations of waveguide height, width, and sidewall angles.

Supplementary Note 3: Electro-mechanical model of HBAR mode

The HBAR used in the experiment in the main text is analyzed using the well-known Modified Butterworth-Van Dyke model (MBVD)[4], which describes the HBAR resonance by an equivalent

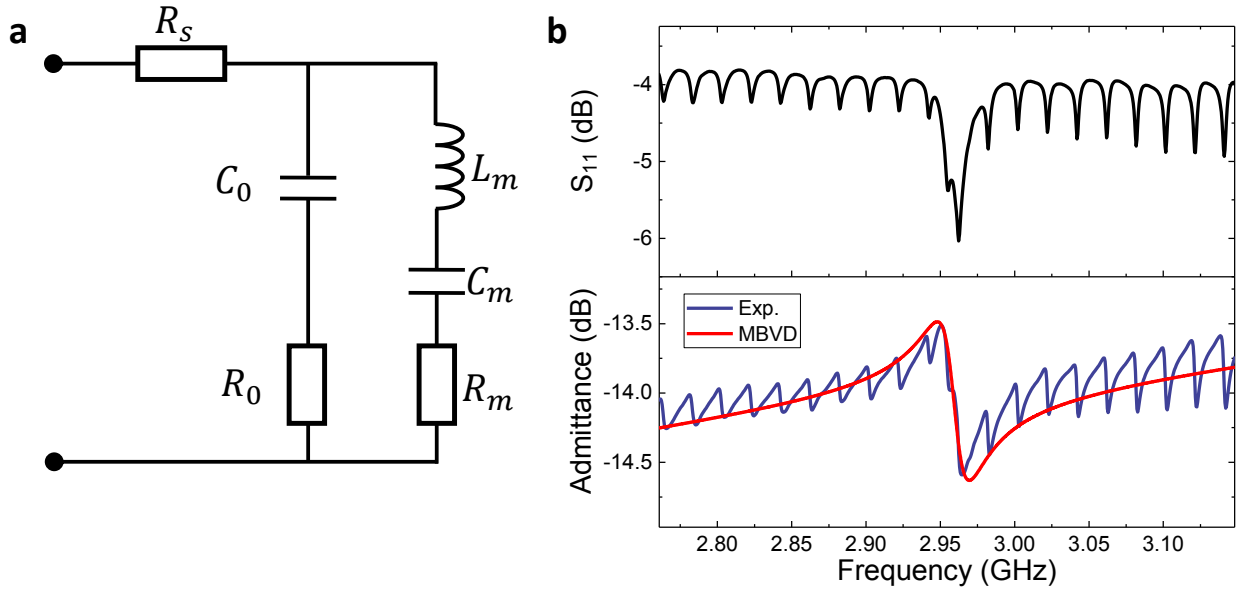

Supplementary Figure 2: Electro-mechanical MBVD model fitting with the HBAR mode. **a** Schematic of equivalent electrical circuit model representing one HBAR mode. **b** Upper panel: electro-mechanical S_{11} around the HBAR mode used in the experiment in the main text. Lower panel: Calculated admittance (blue) and MBVD fitting (red).

Supplementary Table 1: Fitting parameters of MBVD model

C_0	C_m	L_m	R_m	R_0	R_s	$k^2_{t,eff}$	$\omega_m/2\pi$	Q_m
2.137 pF	4.274 fF	0.677 µH	46.8 Ω	45 Ω	47 Ω	0.2 %	2.958 GHz	270

RLC circuit as shown in Supplementary Fig. 2a. L_m and C_m are motional inductance and capacitance which present kinetic and potential energy of the mechanical resonance, while the motional resistance R_m accounts for the intrinsic mechanical loss[5]. The mechanical $R_mL_mC_m$ branch is parallel to a capacitance C_0 that is the physical capacitance formed by the top and bottom electrodes of our piezoelectric actuator. R_0 is the capacitor loss and R_s is the series resistance. The admittance looking into the entire circuit can be calculated as[4]:

$$Y(\omega) = j\omega C_0 \frac{1 - (\frac{\omega}{\omega_p})^2 + j(\frac{\omega}{\omega_p})\frac{1}{Q_{p0}}}{1 - (\frac{\omega}{\omega_s})^2 + j(\frac{\omega}{\omega_s})\frac{1}{Q_{s0}}} \tag{1}$$

where $\omega_s = 1/\sqrt{L_mC_m}$ is the series resonance of the $R_mL_mC_m$ branch, which is also the mechanical resonance. ω_p is the so-called parallel resonance, which is related with ω_s by :

$$\left(\frac{\omega_p}{\omega_s}\right)^2 = 1 + \frac{C_m}{C_0} \tag{2}$$

Q_{s0} and Q_{p0} are the Qs of each resonance:

$$\frac{1}{Q_{s0}} = \omega_s(R_m + R_s)C_m \tag{3}$$

$$\frac{1}{Q_{p0}} = \omega_p(R_0 + R_m)C_m \tag{4}$$

The S_{11} of the HBAR mode around 3 GHz is shown in Supplementary Fig. 2b, from which the admittance can be calculated as:

$$S_{11} = \frac{Z - Z_0}{Z + Z_0} \tag{5}$$

where Z_0 is the impedance of the RF cable which is 50 Ω, and $Z = 1/Y$ is the impedance of the device. The admittance obtained from the S_{11} measurement is then fitted using Eq. 1 as shown in Supplementary Fig. 2b. The fitting parameters are summarized in Supplementary Table 1. The electro-mechanical coupling efficiency $k^2_{t,\text{eff}}$ can be estimated by taking the ratio of capacitance[5] $k^2_{t,\text{eff}} = C_m/C_0$ which is around 0.2 % based on the fitting. The mechanical Q_m can be calculated by $1/(\omega_m R_m C_m)$ which is 270.

Supplementary Note 4: Numerical simulation of RF phase dependency

The RF phase dependency is numerically studied in this section which verifies the experimental data in the main text. The numerical simulation is conducted through a Finite Difference Frequency

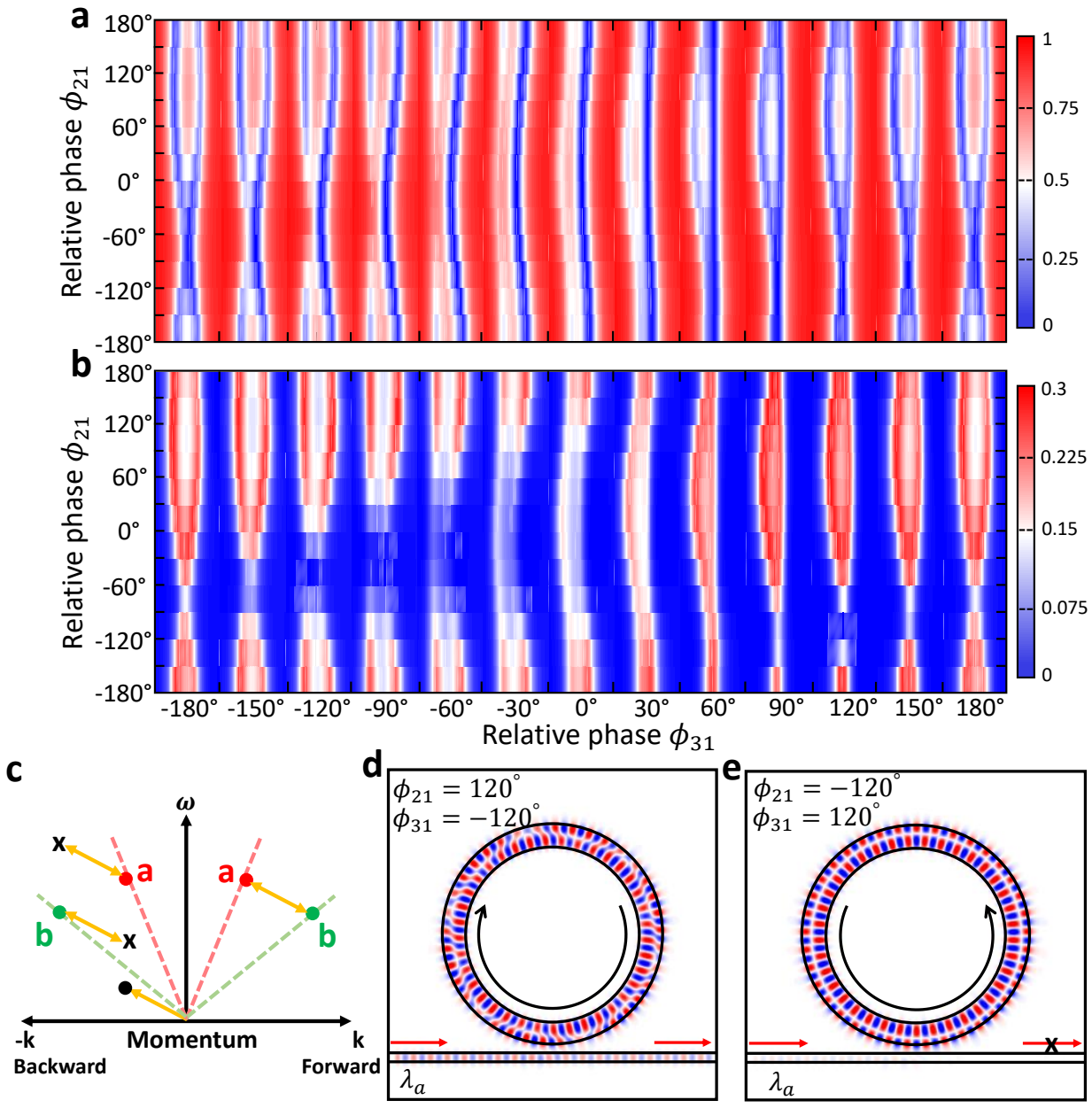

Supplementary Figure 3: FDFD numerical simulation of the RF phase dependency. **a** Transmission spectra of mode a and **b** converted sideband in mode b under 2D sweep of the relative phase ϕ_{21} and ϕ_{31}. It qualitatively agrees with the experimental data in the main text. Each column has a spectra span of (1.5027 nm, 1.5031nm). **c** The $\omega - k$ space showing the relative position of the two optical modes and the rotational modulation wave. Electric field (E_z, out of plane) distribution under reversed phases: **d** $(\phi_{21}, \phi_{31}) = (120°, -120°)$ (perfect phase matching) and **e** $(\phi_{21}, \phi_{31}) = (-120°, 120°)$ (largest phase mismatch). The input light wavelength is at the resonant wavelength of mode a (λ_a = 1502.8 nm). As we change the rotation direction of the modulation wave, the light changes from **d** transmission to **e** isolation.

Domain (FDFD) algorithm developed by Y. Shi *et al*. in Ref.[6,7]. As the optical microresonator used in the experiment is relatively large (118 μm radius) which is time-consuming to simulate, a much smaller optical microring (3 μm radius) is simulated following the same setting as Ref[8], where more structure details and optical properties can be found. It shows similar RF phase dependency behaviour that verifies the experimental data and the numerical model, regardless of the size of the optical microring.

Same as the experiment, the modulation wave need to counter-propagate with the optical modes to satisfy phase matching condition, see Supplementary Fig. 3c. In the simulation, mode a is pumped and mode b is the generated sideband. Different from the previous work[8], the phase (ϕ_{21}, ϕ_{31}) are swept in the simulation, and the 2D plots of the spectra of the transmission of mode a and the conversion of mode b are shown in Supplementary Fig. 3a,b. By comparing with the experiment in the main text, they show qualitative similarity. The light distribution under reversed phases $(\phi_{21}, \phi_{31}) = (120°, -120°)$ (perfect phase matching) and $(\phi_{21}, \phi_{31}) = (-120°, 120°)$ (largest phase mismatch) are shown in Supplementary Fig. 3d,e with fixed input light at the resonance of mode a. Under phase matching as shown in Supplementary Fig. 3d, the light transmits through the bus waveguide, and the electric field in the optical microring is a mixture of modes a and b due to the mode coupling. If the modulation wave's direction is reversed, as shown in Supplementary Fig. 3e, the light is absorbed in the optical microring and the electric field shows the original distribution of mode a, indicting that no mode coupling is induced.

Supplementary Note 5: Measurement of a device with 0.1 dB insertion loss

Another device with 950 nm bus-microring gap is measured which shows an insertion loss of 0.1 dB. The electro- and opto-mechanical properties are characterized in Supplementary Fig. 4a. It shows similar S_{11} as the device presented in the main text, and the mechanical resonances of the actuators also align with each other. Since the optical mode spacing is around 4 GHz for this device, the HBAR at 3.833 GHz is chosen in the experiment. Similar RF phase dependency measurement is conducted as shown in Supplementary Fig. 4b under 20 dBm RF power applied on each actuator. It qualitatively agrees with the simulation in Supplementary Fig. 3c. This device shows larger mode splitting, and maximum of 3.3 GHz is achieved at phase matched case $(\phi_{21}, \phi_{31}) = (-120°, 120°)$. Intriguingly, for phase ϕ_{31} between $-150°$ and $-60°$, there is always mode splitting regardless of ϕ_{21} because of its stronger mode coupling. The optical transmission under reversed phases is shown in Supplementary Fig. 4c. Due to the stronger mode coupling $g/2\pi = 1.65$ GHz, and thus larger optical cooperativity $C \sim 16$, higher optical transmission at center wavelength can be reached around 98%, corresponding to 0.1 dB insertion loss. However, as this device has larger bus-microring coupling gap, the microring is undercoupled to the bus waveguide, leading to less extinction (6 dB) in the backward direction and thus smaller isolation ratio than the device in the main text. Nevertheless, this measurement shows that both low insertion loss (0.1 dB) and high isolation ($>$ 20dB) can be achieved if the bus-microring gap design is optimized in the future.

Supplementary Note 6: Electro-mechanical cross-talk between adjacent actuators

Maintaining small electrical signal cross-talk between adjacent actuators is important for keeping stable relative phases between them. The cross-talk is measured by driving actuator 1 and detecting

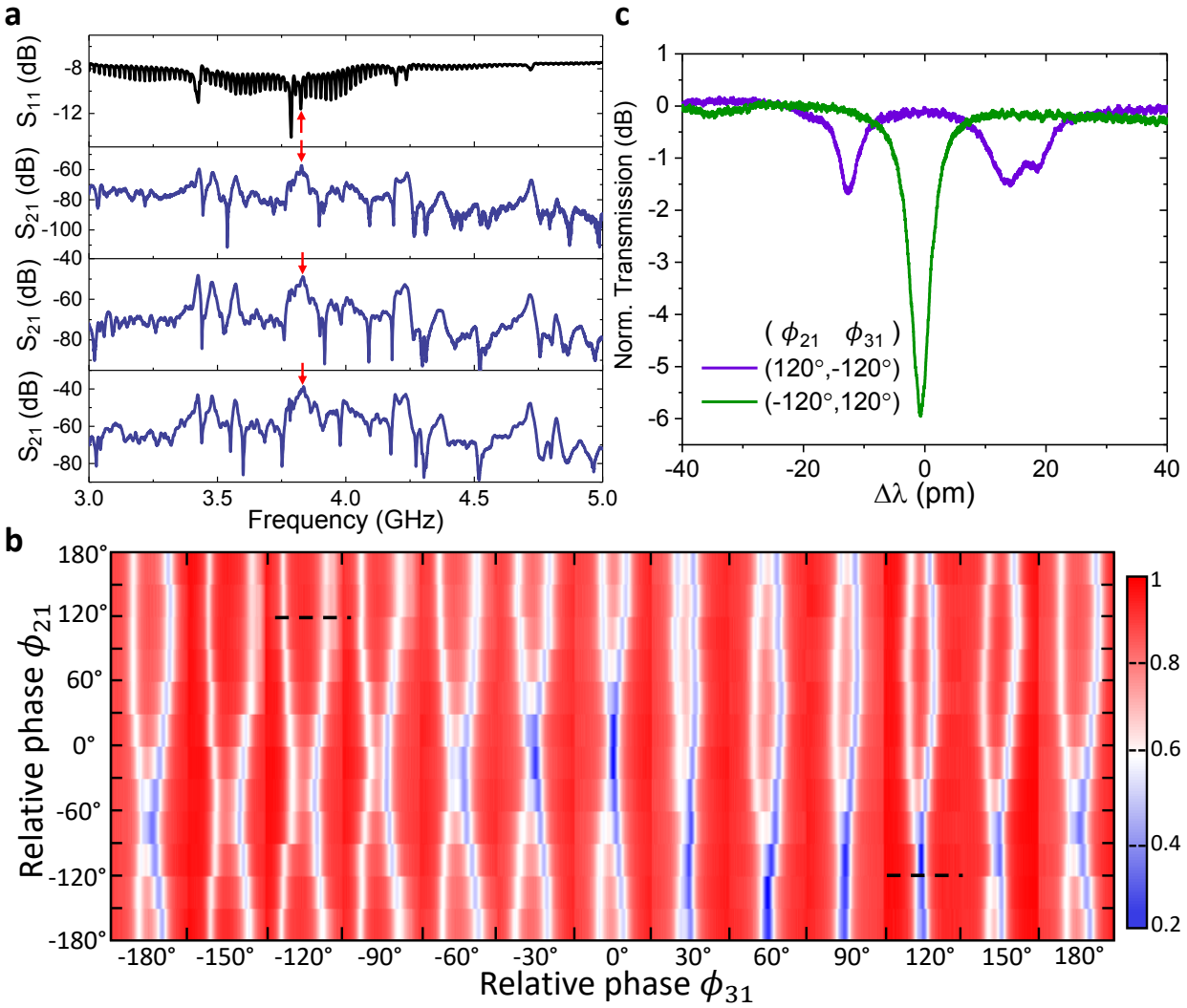

Supplementary Figure 4: Characterization of the device with 0.1 dB insertion loss. **a** From top to bottom are microwave reflection S_{11}, optomechanical response S_{21} of the three actuators 1, 2, and 3, respectively. Red arrows mark the mechanical mode at 3.833 GHz that is used in the experiment. **b** Normalized optical transmission of the TE_{00} mode under 2D sweep of phases of signals 2 and 3 relative to signal 1, i.e. sweeping ϕ_{21} and ϕ_{31}. Each column is the measured spectrum under the same ϕ_{31} with spectral span of $\pm$24 pm relative to the center wavelength λ_0 (1553 nm) of the TE_{00} mode. **c** Optical transmission spectra along black dashed lines in **b** with reversed phases: $(\phi_{21}, \phi_{31}) = (120°, -120°)$ (perfect phase matching) and $(\phi_{21}, \phi_{31}) = (-120°, 120°)$ (largest phase mismatch).

the output electrical signal from actuators 1 (S_{11}), 2 (S_{21}), and 3 (S_{31}), as shown in Supplementary Fig. 5. Due to the rotational symmetry of the device, the cases for driving actuators 2 and 3 individually are similar. From the results, we can see that the cross-talk is well maintained below -60 dB over the measured range of 1 to 6 GHz, which means that the cross-talk from adjacent actuators is 6 orders of magnitude smaller than the signal applied. The low cross-talk mainly comes from the tight acoustic wave confinement and the center release hole that prevents lateral acoustic waves from propagating. The variation of envelope is mainly from the background noise (gray) which is measured by lifting the probes.

Supplementary Note 7: Thermal heating effects due to high RF power

As discussed in the main text, the thermal heating effect of RF power leads to fast transition from low g at 17 dBm to high g at 18 dBm. Here, how this transition takes place is studied in details by fine RF power sweep between 17 and 18 dBm, as shown in Supplementary Fig. 6a. The fine sweep connects the low and high RF power data set. The sweep is conducted back and forth, and no obvious hysteresis is observed. To further explain the origin of the heating effects, electro-mechanical S_{11} is measured under different RF powers as shown in Supplementary Fig. 6b. It can be seen clearly that the SiO_2 HBAR is blue-shifted when the RF power increases from -5 dBm to 18 dBm. Intriguingly, due to the better thermal conductance of the Si substrate, the Si HBARs show no prominent shift, which also verifies that the blue shift of SiO_2 HBAR is not from

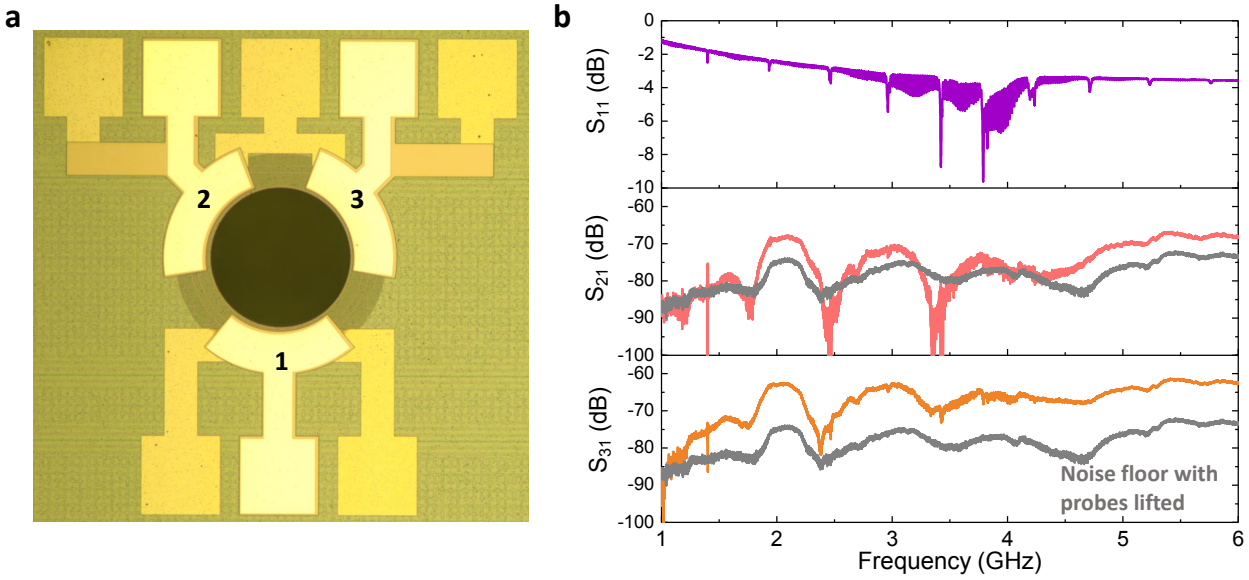

Supplementary Figure 5: Electro-mechanical cross-talk between adjacent actuators. **a** Optical microscope image of the device. Three actuators are as labeled. **b** Electro-mechanical S_{11} (purple), electrical cross-talk between actuators 2 and 1 S_{21} (pink), and 3 and 1 S_{31} (yellow). The noise floor with probes lifted (gray) is shown for reference.

measurement errors. The blue shift of the SiO_2 HBAR is mainly from the bad thermal conductance of the free-standing SiO_2 membrane and the large temperature coefficient of elasticity of SiO_2. The shift of HBAR resonances will introduce phase shift on the modulation, which can be actively compensated by adjusting the RF signal phases experimentally.

The power handling capability of our piezoelectric actuators is also studied. For RF power under 27 dBm, the piezoelectric actuator can work continuously for several hours without degradation. However, for RF power higher than 30 dBm, there is gradual roughening of the top electrode surface, as seen in Supplementary Fig. 7a. Also, there is burning at the sharp corners of the bottom electrode which is caused by the current crowding under high RF power. Interestingly, the outer edge of the rough region aligns with the edge of the undercut (black line), indicating that the degradation is mainly due to the low thermal conductivity of the suspended SiO_2 membrane. Also, the degradation is split by three concentric circles into several regions which align with the underneath Si_3N_4 microring waveguide and dummy ring structures (blue lines) designed for uniform chemical-mechanical polishing (CMP). This is likely due to that these Si_3N_4 structures scatter the acoustic waves which reduces the energy density around these regions. The roughness is highlighted in the SEM images in Supplementary Fig. 7b,c. The top Al layer is corrugated and detached from AlN. One possible reason for this detachment is that the large vertical displacement and vibration under high power loosen the adhesion of Al to AlN. This may explain why the Si_3N_4 region is not influenced since the acoustic energy is dissipated by the scattering. So the corrugation of Al may "undesirablely" maps the distribution of acoustic mode.

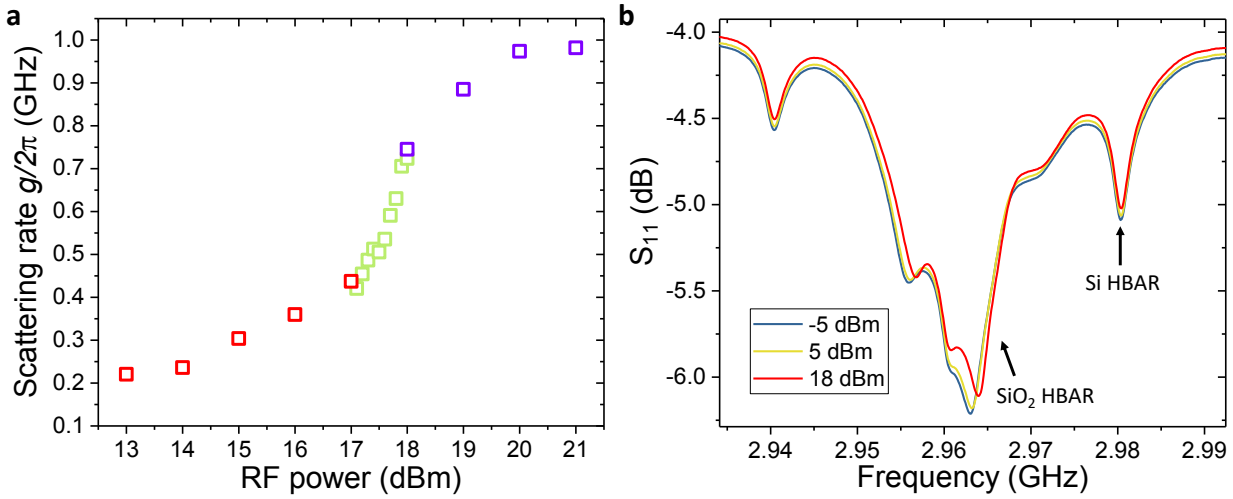

Supplementary Figure 6: Thermal heating of RF power. **a** Scattering rate g at different RF power. Green squares are fine sweep between 17 to 18 dBm with 0.1 dBm step. Red and purple squares correspond to the same data in the main text. **b** Electro-mechanical S_{11} under different RF power around the HBAR mode used in the main text. The resonances of SiO_2 and Si HBARs are as labeled.

Supplementary Note 8: Influence of sideband generation due to temporal modulation

The generated sideband can be problematic if not fully filtered. Supplementary Figure 8a plots together the TE light and TM sideband after splitting by the polarization beam splitter (PBS) under 20 dBm RF power on each actuator. Due to the mode splitting, the conversion to TM sideband is suppressed within a window around the center resonance ($\Delta f = 0$), which is ~ 15 dB smaller.

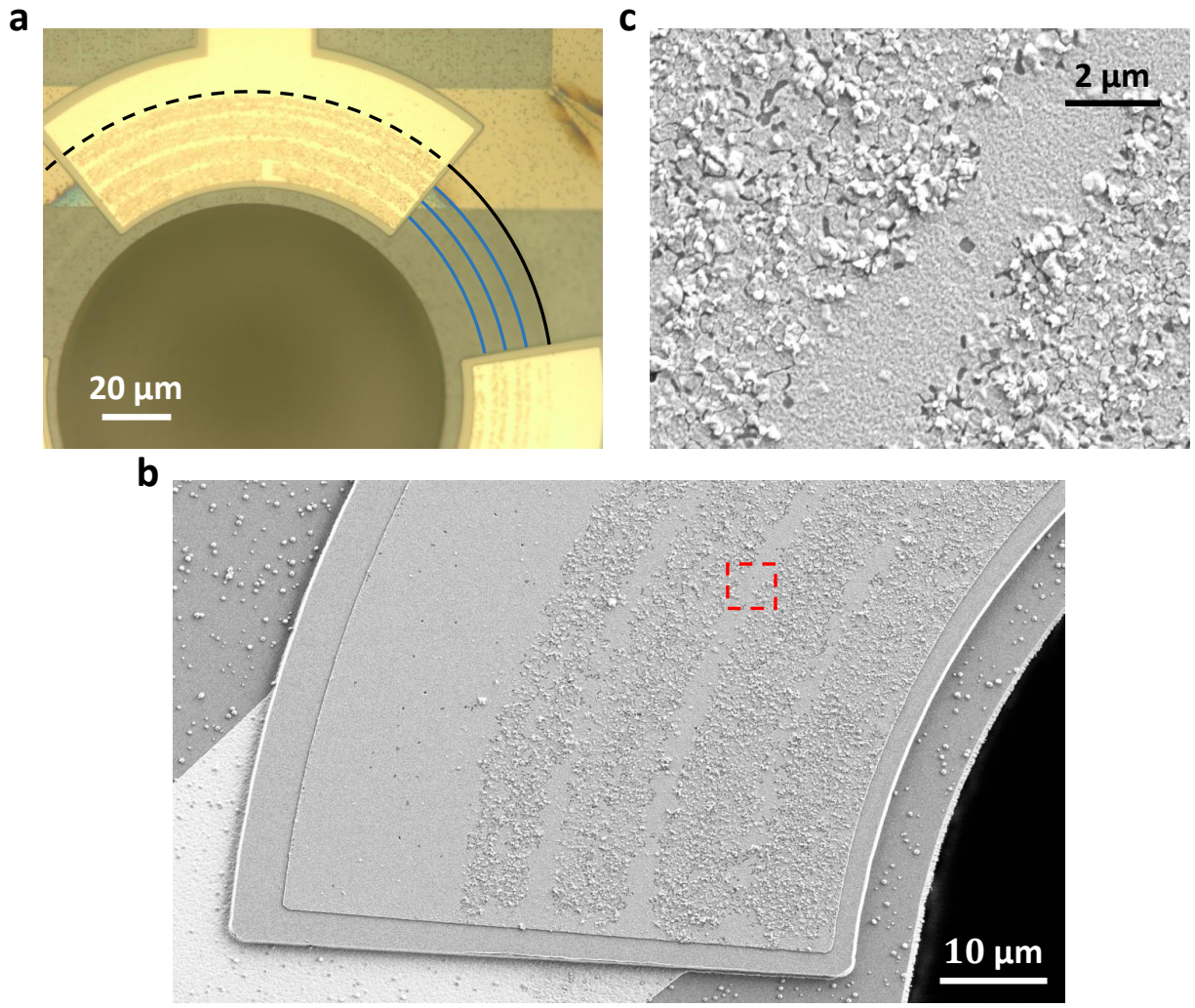

Supplementary Figure 7: Degradation of the actuator under 30 dBm RF power. **a** Optical microscope image of the device undergoes 30 dBm RF power. Black line denotes the edge of the SiO_2 undercut. Blue lines outlines the Si_3N_4 microring waveguide and dummy waveguides. **b** SEM image showing the corrugated surface of the Al top electrode. **c** Zoom-in SEM of the region in the red dashed box in **b**.

The conversion efficiency (at $\Delta f = 0$) can be calculated as:

$$\eta = \frac{\kappa_{a,\mathrm{ex}}}{\kappa_a}\frac{\kappa_{b,\mathrm{ex}}}{\kappa_b}\frac{4C}{(1+C)^2} \tag{6}$$

We can see that when $C \gg 1$, the conversion is inversely proportional to C. Thus we can suppress the TM sideband by increasing RF power. Furthermore, the sideband can be suppressed by making the TM mode undercoupled, i.e. $\kappa_{b,\mathrm{ex}} \ll \kappa_b$. This has been demonstrated in Ref.[9] on integrated $LiNbO_3$ optical isolators where one mode is specifically designed to be undercoupled.

To directly probe the sideband, we measured the output spectrum using an optical spectrum analyzer (OSA) before and after the PBS with a fixed input laser frequency. First, because the optical mode spacing and RF drive frequency (2 to 4 GHz) are larger than the optical linewidth (< 1 GHz), we are in the sideband resolved regime. This enables single sideband modulation, as shown in the spectrum before PBS in Supplementary Fig. 8b. Second, the PBS filters out TM effectively as illustrated in Supplementary Fig. 8b. The fiber PBS useded here (Thorlab PBC1550SM-FC) has > 20 dB extinction ratio between TE and TM. Therefore, the influence of TM sideband on the output signal is negligible.

The purity of the output signal is further confirmed by comparing with the spectrum when RF is off (yellow line in Supplementary Fig. 8b). There is no frequency shift within the resolution of the OSA. The only limitation on the signal quality can be the finite bandwidth of the optical resonance. We have conducted time-domain measurement with input optical pulses. As long as the signal bandwidth is within the resonance bandwidth, no prominent signal distortion is observed as shown in Supplementary Fig. 8c.

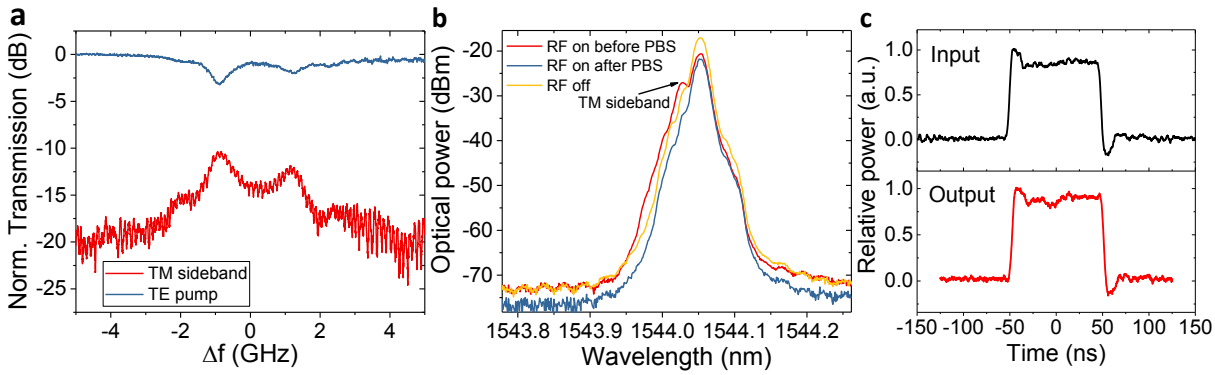

Supplementary Figure 8: Influence of sideband generation on output signal purity. **a** Normalized optical transmission of the TE pump (blue) and the TM sideband (red). The TM sideband is 15 dB weaker than the TE pump. **b** Output optical spectra with a fixed input laser frequency when RF power is on and off. The spectra before and after the PBS are measured, showing the single sideband generation and the effectiveness of PBS for filtering out TM light. **c** Input and output optical pulses through our isolator with 100 ns pulse duration.

Supplementary Note 9: Results from an over-coupled device with 600 nm gap

Another device of 600 nm coupling gap is characterized as shown in Supplementary Fig. 9a. In this case, the device works in the opposite way: 1. As the device is over-coupled, it shows high transmission when there is no mode coupling induced in the phase-mismatched direction; 2. In the phase-matched direction, mode coupling converts the input light into the other auxiliary mode and finally gets filtered. The advantage of this approach is the amount of light converted into the other mode can be controlled by the RF power. This can also be understood intuitively that the conversion to the other mode effectively increases the microresonator intrinsic loss, and critical coupling can be achieved by matching the intrinsic loss with the external coupling rate. Maximum of 43.3 dB extinction is obtained at -0.75 GHz laser detuning, with -1.86 dB transmission at phase-mismatched case (red curve), corresponding to an isolation ratio of 41 dB. Due to the lower optical Q for over-coupled device, the modulation efficiency is reduced and the requires RF power is higher than that used for the under-coupled device in the main text. The extinction gradually increases with increasing RF power, and mode starts splitting over 28 dBm. Applying higher RF power is avoided as the AlN actuator starts to degrade. On the other hand, the lower optical Q helps to achieve larger isolation bandwidth as shown in Supplementary Fig. 9c. Isolation larger than 20 dB is obtained over 2 GHz bandwidth. Strategies to reduce RF power are discussed in the next section.

As mentioned in the main text, conversion to the TM sideband can have higher efficiency, which is studied in Supplementary Fig. 9b. Maximum of 60% conversion is achieved which can be further increased in devices that are more over-coupled. This device integrates three features together: frequency shifting, polarization rotating, and non-reciprocity, which can find applications in frequency-encoded quantum optical computing[10,11].

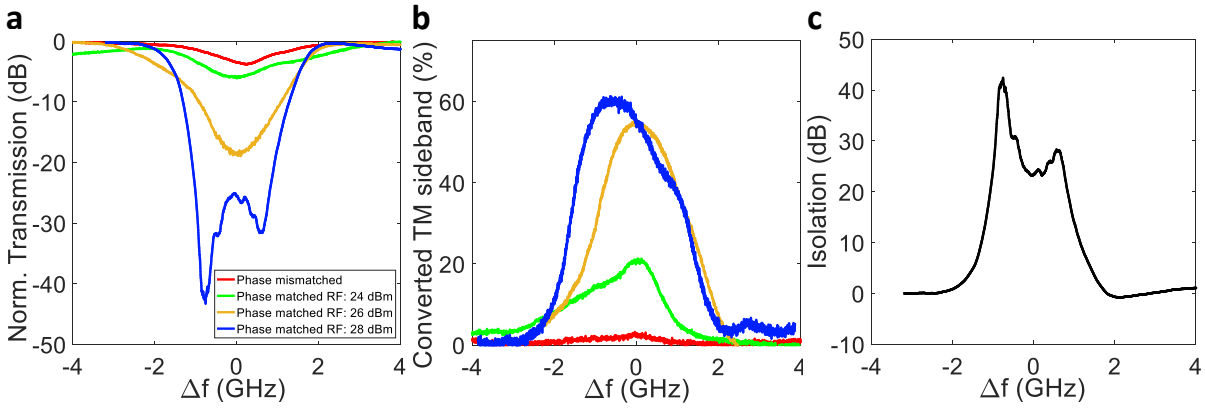

Supplementary Figure 9: Isolation and sideband generation of the over-coupled device with 600 nm gap. **a** Normalized optical transmission in the phase-mismatched case (red) and phase-matched cases with increasing RF power applied on each actuator (green, yellow, blue). **b** Conversion to the TM mode under each setting in **a**. **c** Isolation ratio by taking difference between the phase-matched case under 28 dBm (blue) and mismatched case (red) in **a**.

Supplementary Note 10: Comparison with current optical non-reciprocal devices

This section reviews and summarizes most recent optical non-reciprocal devices realized using different schemes, and compares their performance with our work in Supplementary Table 2. The isolation and insertion loss of these devices are summarized and plotted in Supplementary Fig. 10 for better visualization. Optical non-reciprocal devices have long been realized using magneto-optic materials with the Faraday effect. However, it is challenging to integrate these materials as they are not compatible with most CMOS processes. Nevertheless, there have been advancements towards integrating cerium-substituted yttrium iron garnet (Ce:YIG) on Si photonic chips via wafer bonding[12]. Most recently, Ce:YIG has been grown on silicon nitride by pulsed laser deposition (PLD)[13]. However, it still needs bulky external magnet to generate the required magnetic field to break the Lorentz reciprocity. On the other hand, in the applications for building optical interfaces to connect distant superconducting circuits for quantum internet[27], the applied external magnetic

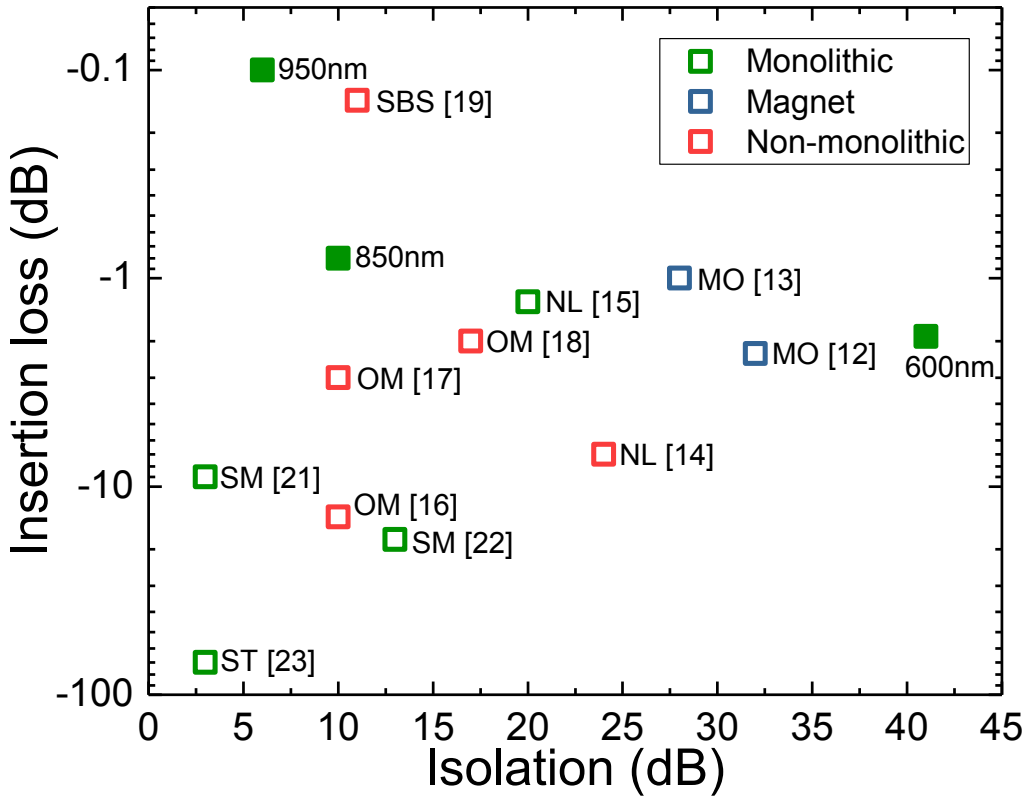

Supplementary Figure 10: Comparison of insertion loss and isolation among several experimental realizations of optical isolators. These devices are classified by the level of integration into monolithic (green), and non-monolithic (red). Devices relying on magneto-optic material (blue) is separately listed while others are all magnetic-free. The three devices with 950, 850, and 600 nm gaps shown in this work are listed separately as solid green squares. The references are as labeled.

Supplementary Table 2: Comparison of optical non-reciprocal devices realized using different schemes: MO (magneto-optic), NL (nonlinear optics), OM (optomechanical), SBS (stimulated Brillouin scattering), SM (synthetic magnetic field), and ST (spatio-temporal modulation). IL: Insertion loss. The three devices with 950, 850, and 600 nm gaps shown in this work are listed separately. A commercial bulk optical isolator is listed for comparision. a: Non-reciprocal sideband modulation. b: Optical pump power.

Year	Scheme	Structure	Material	Isolation	IL (dB)	Bandwidth	Power	CMOS
2016[12]	MO	Ring	Si+Ce:YIG	32 dB	2.3	15 GHz	10 mW	No
2020[13]	MO	Ring	SiN+Ce:YIG	28 dB	1	15 GHz		No
2018[14]	NL	Toroid	SiO_2	24 dB	7	1 MHz	No drive	No
2020[15]	NL	Ring	Si	20 dB	1.3	20 GHz	No drive	Yes
2016[16]	OM	Toroid	SiO_2	10 dB	14	250 kHz	17 μW^b	No
2018[17]	OM	Toroid	SiO_2	10 dB	3	60 kHz	60 μW^b	No
2018[18]	OM	Sphere	SiO_2	17 dB	2	200 kHz	7.8 mW^b	No
2017[19]	SBS	Sphere	SiO_2	11 dB	0.14	400 kHz	235 μW^b	No
2014[20]	SM	MZI	Doped Si	2.4 dB		20 nm	34 dBm	Yes
2021[21]	SM	Ring	AlN	3 dB	9	4 GHz	16 dBm	Yes
2021[22]	SM	Ring	Doped Si	13 dB	18	2 GHz	-3 dBm	Yes
2012[23]	ST	MZI	Doped Si	3 dB	70	200 GHz	25 dBm	Yes
2018[24]	ST^a	MZI	Si	39 dB	NA	125 GHz	90 mW^b	Yes
2018[25]	ST^a	Ring	AlN	15 dB	NA	1 GHz	18 dBm	Yes
2021[26]	ST^a	MZI	Si+AlN	16 dB	NA	100 GHz	21 dBm	Yes
850 nm	ST	Ring	Si_3N_4+AlN	10 dB	0.8	0.7 GHz	25 dBm	Yes
950 nm	ST	Ring	Si_3N_4+AlN	6 dB	0.1	0.7 GHz	25 dBm	Yes
600 nm	ST	Ring	Si_3N_4+AlN	41 dB	1.9	2 GHz	33 dBm	Yes
Thorlab	IO-K-1550			35 dB	1.2	40 nm		No

field would unavoidably interfere the operation of superconducting qubits. Thus, magnetic-free optical isolators are especially desired in this case.

Optical non-reciprocity has been demonstrated in optomechanical systems through optomechanically induced transparency (OMIT)[16–18,28], where an optical pump in one optical mode excites and couples a mechanical resonance with another optical mode. However, most of these demonstrations are realized in a stand-alone optical microresonator (microtoroid or microsphere) that supports both optical and mechanical whispering gallery modes (WGMs). This scheme is difficult to integrate with PICs in a convenient and reliable manner. Moreover, as it requires optical pump, the power of the probe light has to be much smaller than the pump light to maintain stable optomechanical interaction. This limits the dynamic range of the optical power that can be isolated. On the other hand, in OMIT the bandwidth of the transparency window is limited by the mechanical linewidth, which limits the isolation bandwidth to below megahertz (see Supplementary Table 2).

Other monolithic integrated optical non-reciprocal devices are realized either by optical nonlinearity or by dynamical modulation (spatio-temporal modulation and synthetic magnetic field), benefit-

ing from the advanced integration of nonlinear components[29] and electro-optic and acousto-optic modulators[30–37]. The recent work[15] using the Si nonlinearity has achieved 20 dB isolation and 20 GHz bandwidth. However, the fact that it works for optical power within 4 to 8 dBm limits its applications. In contrast, dynamic modulation, especially with electrical driving, largely preserves the optical linearity by separating driving and sensing in two different domains. The early experiments[20,23] are based on modulating doped-Si waveguides in a Mach-Zehnder interferometer (MZI). However, the exaggerated loss of the doped-Si waveguides (70 dB insertion loss) limits the maximum isolation within 2.4 to 3 dB. Recently, spatio-temporal modulation using AOM has been implemented[24–26]. Limited by either the modulation efficiency or the power handling capability of electrodes, complete mode conversion ($C = 1$) has not been achieved, i.e. only non-reciprocal sideband modulation is demonstrated. Most recently, optical isolators are demonstrated by modulating coupled optical microrings through either synthetic Hall effect[21] or Aharonov-Bohm effect[22], but with limited isolation[21] and large insertion loss[22]. In comparison, our HBAR resonator shows better power handling capability because of its wide electrode area (and thus small resistance). Also, the tight confinement of acoustic energy in thin SiO_2 membrane improves the modulation efficiency by 100 times compared with previous unreleased Si HBARs[33]. With these features, we demonstrate the lowest insertion loss among these works, and comparable isolation under reasonable amount of RF power applied.

Supplementary Note 11: Outlook on future applications and improvements

In practical applications, the main figure of merit for an isolator is its insertion loss, isolation ratio and bandwidth. We summarize in Supplementary Table 2 the comparison of our current devices with a commercial bulk isolator from Thorlab IO-K-1550. The critically coupled device (950 nm gap) have 0.1 dB insertion loss, while the isolation ratio is limited by the critical coupling level of the microring. In the current fabrication, we sweep the bus-microring gap distance coarsely with 50 nm step. In the future, finer gap sweep can be implemented for better critical coupling. Experimentally, 30 dB extinction can be achieved, which is comparable with most commercial isolators. On the other hand, due to the low insertion loss, cascading several isolators can increase isolation. For example, by cascading five 950-nm-gap devices, we can have 30 dB isolation and 0.5 dB insertion loss. The over-coupled 600-nm-gap device shows higher isolation and higher insertion loss than the commercial isolator.

The bandwidth is limited by the optical resonance linewidth. The isolator bandwidth can be increased by either increasing the microresonator's intrinsic loss, or increasing the external coupling rate by working in the over-coupling regime. This however increases the RF power consumption. Nevertheless, there are still ways to reduce the RF power in the future. The piezo-optomechanical coupling efficiency is mainly determined by the cooperativity C:

$$C = \frac{4g_0^2}{\kappa_a \kappa_b} n_c \tag{7}$$

Based on the expression, there are some strategies to increase C:

- **Reducing the optical microring radius**. This is an effective way to increase the g_0 by shrinking both of the optical and mechanical mode volume[5]. For optical microring with 22 μm radius, the mechanical mode volume will be decreased by 25 times. As the g_0 is inversely proportional to the square root of volume, this leads to 25 times decreasing of RF power to 12 mW.

- **Using scandium (Sc) doped AlN**. AlScN has 4 times larger piezoelectric coefficient than that of AlN[38]. If using AlScN, we anticipate at least 4 times increase of electro-mechanical coupling, leading to 4 times reduction of the RF power.

- **Increasing optical** Q. This can be achieved using our optimized photonic Damascene process[3]. We expect to achieve 100 MHz optical resonance linewidth ($Q = 2 \times 10^6$). This would lead to RF power reduction to 6 mW. However, there is a trade-off between isolation bandwidth and RF power. Additionally, if microresonators of $Q > 10^7$ are used, the higher intra-cavity power boosted by higher Q will induce large resonance shift due to thermal-optic and Kerr nonlinearity. In this case, the resonance shift caused by high input power of the optical signal will be prominent, which will affect the device performance.

- **Increasing mechanical** Q. This will increase the intra-cavity phonon number under the same input microwave. Currently our mechanical Q is limited by the acoustic energy leakage into the HBAR mode within the substrate. In the future, the substrate HBAR can be eliminated by roughening the backside surface of the substrate as demonstrated in our previous work[33]. We anticipate at least two times improvement of mechanical Q.

We estimate that a combination of these strategies could reduce the required RF power to $\sim$ 60 μW.

Isolators protect lasers from back-reflection and maintain unidirectional transmission of light signals. Recently, there are several demonstrations of self-injection locking of an integrated laser to a Si_3N_4 microresonator[39,40]. Laser self-injection locking enables direct interaction of the laser and the microresonator through back-scattered light from the microresonator, where an optical isolator is absent. However, an integrated optical isolator between the laser and the microresonator is still preferred in certain circumstances that full laser control is required. For example, Ref.[41] shows that an isolator between the semiconductor laser and the Si_3N_4 microresonator is needed to increase the optical bandwidth of the generated soliton comb. In this case, an optical isolator of few hundreds of megahertz bandwidth (as our case) is sufficient to cover the laser tuning range for soliton comb generation.

Due to the resonant nature of the optical microresonator, the bandwidth is limited by the optical resonance linewidth. The current bandwidth of our device ($\sim$ 700 MHz) is sufficient for applications such as microwave to optical converters for quantum interconnects[27] and classical optical readout of superconducting qubits' states[42], where the qubit Rabi oscillation is usually on the order

of tens of megahertz. The main limitation in these applications is the RF power consumption. In current commercial dilution fridges, the cooling power at 50 K and 4 K stages are 50 W and 1.5 W, respectively. The RF power consumption of our devices can be further reduced to meet the cooling power budget.

In summary, we believe that < 1 dB insertion loss and > 30 dB isolation can be achieved by optimizing our designs. Together with RF power of less than 1 mW, our integrated optical isolators can meet the requirements for many applications for nonlinear photonics and quantum engineering in the future.

References

1. Pfeiffer, M. H. P. *et al.* Photonic damascene process for low-loss, high-confinement silicon nitride waveguides. *IEEE J. Sel. Top. Quantum Electron.* **24**, 1–11 (2018).

2. Liu, J. *et al.* Ultralow-power chip-based soliton microcombs for photonic integration. *Optica* **5**, 1347–1353 (2018). URL http://www.osapublishing.org/optica/abstract.cfm?URI=optica-5-10-1347.

3. Liu, J. *et al.* High-yield, wafer-scale fabrication of ultralow-loss, dispersion-engineered silicon nitride photonic circuits. *Nature Communications* **12**, 2236 (2021). URL https://doi.org/10.1038/s41467-021-21973-z.

4. Larson, J. D., Bradley, P. D., Wartenberg, S. & Ruby, R. C. Modified butterworth-van dyke circuit for fbar resonators and automated measurement system. In *2000 IEEE Ultrasonics Symposium. Proceedings. An International Symposium (Cat. No. 00CH37121)*, vol. 1, 863–868 (IEEE, 2000).

5. Blésin, T., Tian, H., Bhave, S. & Kippenberg, T. Quantum coherent microwave-optical transduction using high overtone bulk acoustic resonances. *arXiv* **2103.00471** (2021).

6. Shi, Y., Shin, W. & Fan, S. Multi-frequency finite-difference frequency-domain algorithm for active nanophotonic device simulations. *Optica* **3**, 1256–1259 (2016). URL http://www.osapublishing.org/optica/abstract.cfm?URI=optica-3-11-1256.

7. Shi, Y. Two-dimensional finite-difference frequency-domain (fdfd) programs (2018). URL https://github.com/YuJerryShi/fdfd_suite.

8. Shi, Y., Lin, Q., Minkov, M. & Fan, S. Nonreciprocal optical dissipation based on direction-dependent rabi splitting. *IEEE J. Sel. Top. Quantum Electron.* **24**, 1–7 (2018).

9. Sohn, D., Örsel, O. E. & Bahl, G. Electrically driven linear optical isolation through phonon mediated autler-townes splitting. *arXiv preprint arXiv:2104.04803* (2021).

10. Hu, Y. *et al.* Reconfigurable electro-optic frequency shifter. *arXiv* **2005.09621** (2020).

11. Arrazola, J. M. *et al.* Quantum circuits with many photons on a programmable nanophotonic chip. *Nature* **591**, 54–60 (2021). URL https://doi.org/10.1038/s41586-021-03202-1.

12. Huang, D. *et al.* Electrically driven and thermally tunable integrated optical isolators for silicon photonics. *IEEE J. Sel. Top. Quantum Electron.* **22**, 271–278 (2016).

13. Yan, W. *et al.* Waveguide-integrated high-performance magneto-optical isolators and circulators on silicon nitride platforms. *Optica* **7**, 1555–1562 (2020). URL http://www.osapublishing.org/optica/abstract.cfm?URI=optica-7-11-1555.

14. Bino, L. D. *et al.* Microresonator isolators and circulators based on the intrinsic nonreciprocity of the kerr effect. *Optica* **5**, 279–282 (2018). URL http://www.osapublishing.org/optica/abstract.cfm?URI=optica-5-3-279.

15. Yang, K. Y. *et al.* Inverse-designed non-reciprocal pulse router for chip-based lidar. *Nature Photonics* **14**, 369–374 (2020). URL https://doi.org/10.1038/s41566-020-0606-0.

16. Ruesink, F., Miri, M.-A., Alù, A. & Verhagen, E. Nonreciprocity and magnetic-free isolation based on optomechanical interactions. *Nature Communications* **7**, 13662 (2016). URL https://doi.org/10.1038/ncomms13662.

17. Ruesink, F., Mathew, J. P., Miri, M.-A., Alù, A. & Verhagen, E. Optical circulation in a multimode optomechanical resonator. *Nature Communications* **9**, 1798 (2018). URL https://doi.org/10.1038/s41467-018-04202-y.

18. Shen, Z. *et al.* Reconfigurable optomechanical circulator and directional amplifier. *Nature Communications* **9**, 1797 (2018). URL https://doi.org/10.1038/s41467-018-04187-8.

19. Kim, J., Kim, S. & Bahl, G. Complete linear optical isolation at the microscale with ultralow loss. *Scientific Reports* **7**, 1647 (2017). URL https://doi.org/10.1038/s41598-017-01494-w.

20. Tzuang, L. D., Fang, K., Nussenzveig, P., Fan, S. & Lipson, M. Non-reciprocal phase shift induced by an effective magnetic flux for light. *Nature Photonics* **8**, 701–705 (2014). URL https://doi.org/10.1038/nphoton.2014.177.

21. Kim, S., Sohn, D. B., Peterson, C. W. & Bahl, G. On-chip optical non-reciprocity through a synthetic hall effect for photons. *APL Photonics* **6**, 011301 (2021). URL https://doi.org/10.1063/5.0034291.

22. Dostart, N., Gevorgyan, H., Onural, D. & Popović, M. A. Optical isolation using microring modulators. *Opt. Lett.* **46**, 460–463 (2021). URL http://ol.osa.org/abstract.cfm?URI=ol-46-3-460.

23. Lira, H., Yu, Z., Fan, S. & Lipson, M. Electrically driven nonreciprocity induced by interband photonic transition on a silicon chip. *Phys. Rev. Lett.* **109**, 033901 (2012). URL https://link.aps.org/doi/10.1103/PhysRevLett.109.033901.

24. Kittlaus, E. A., Otterstrom, N. T., Kharel, P., Gertler, S. & Rakich, P. T. Non-reciprocal interband brillouin modulation. *Nature Photonics* **12**, 613–619 (2018). URL https://doi.org/10.1038/s41566-018-0254-9.

25. Sohn, D. B., Kim, S. & Bahl, G. Time-reversal symmetry breaking with acoustic pumping of nanophotonic circuits. *Nature Photonics* **12**, 91–97 (2018). URL https://doi.org/10.1038/s41566-017-0075-2.

26. Kittlaus, E. A. *et al.* Electrically driven acousto-optics and broadband non-reciprocity in silicon photonics. *Nature Photonics* **15**, 43–52 (2021). URL https://doi.org/10.1038/s41566-020-00711-9.

27. Awschalom, D. *et al.* Development of quantum interconnects (quics) for next-generation information technologies. *PRX Quantum* **2**, 017002 (2021). URL https://link.aps.org/doi/10.1103/PRXQuantum.2.017002.

28. Shen, Z. *et al.* Experimental realization of optomechanically induced non-reciprocity. *Nature Photonics* **10**, 657–661 (2016). URL https://doi.org/10.1038/nphoton.2016.161.

29. Kovach, A. *et al.* Emerging material systems for integrated optical kerr frequency combs. *Adv. Opt. Photon.* **12**, 135–222 (2020). URL http://aop.osa.org/abstract.cfm?URI=aop-12-1-135.

30. Melikyan, A. *et al.* High-speed plasmonic phase modulators. *Nature Photonics* **8**, 229–233 (2014). URL https://doi.org/10.1038/nphoton.2014.9.

31. Wang, C. *et al.* Integrated lithium niobate electro-optic modulators operating at cmos-compatible voltages. *Nature* **562**, 101–104 (2018). URL https://doi.org/10.1038/s41586-018-0551-y.

32. He, M. *et al.* High-performance hybrid silicon and lithium niobate mach–zehnder modulators for 100 gbit s-1 and beyond. *Nature Photonics* **13**, 359–364 (2019). URL https://doi.org/10.1038/s41566-019-0378-6.

33. Tian, H. *et al.* Hybrid integrated photonics using bulk acoustic resonators. *Nature Communications* **11**, 3073 (2020). URL https://doi.org/10.1038/s41467-020-16812-6.

34. Chen, L., Xu, Q., Wood, M. G. & Reano, R. M. Hybrid silicon and lithium niobate electro-optical ring modulator. *Optica* **1**, 112–118 (2014). URL http://www.osapublishing.org/optica/abstract.cfm?URI=optica-1-2-112.

35. Tadesse, S. A. & Li, M. Sub-optical wavelength acoustic wave modulation of integrated photonic resonators at microwave frequencies. *Nature Communications* **5**, 5402 (2014). URL https://doi.org/10.1038/ncomms6402.

36. Shao, L. *et al.* Microwave-to-optical conversion using lithium niobate thin-film acoustic resonators. *Optica* **6**, 1498–1505 (2019). URL http://www.osapublishing.org/optica/abstract.cfm?URI=optica-6-12-1498.

37. Tian, H. *et al.* X-band aom on chip. In *2021 IEEE 34th International Conference on Micro Electro Mechanical Systems (MEMS)*, 210–213 (2021).

38. Pirro, M. *et al.* Characterization of dielectric and piezoelectric properties of ferroelectric alscn thin films. In *2021 IEEE 34th International Conference on Micro Electro Mechanical Systems (MEMS)*, 646–649 (IEEE, 2021).

39. Shen, B. *et al.* Integrated turnkey soliton microcombs. *Nature* **582**, 365–369 (2020). URL https://doi.org/10.1038/s41586-020-2358-x.

40. Voloshin, A. S. *et al.* Dynamics of soliton self-injection locking in optical microresonators. *Nature Communications* **12**, 235 (2021). URL https://doi.org/10.1038/s41467-020-20196-y.

41. Briles, T. C. *et al.* Hybrid inp and sin integration of an octave-spanning frequency comb. *APL Photonics* **6**, 026102 (2021).

42. Youssefi, A. *et al.* A cryogenic electro-optic interconnect for superconducting devices. *Nature Electronics* **4**, 326–332 (2021). URL https://doi.org/10.1038/s41928-021-00570-4.